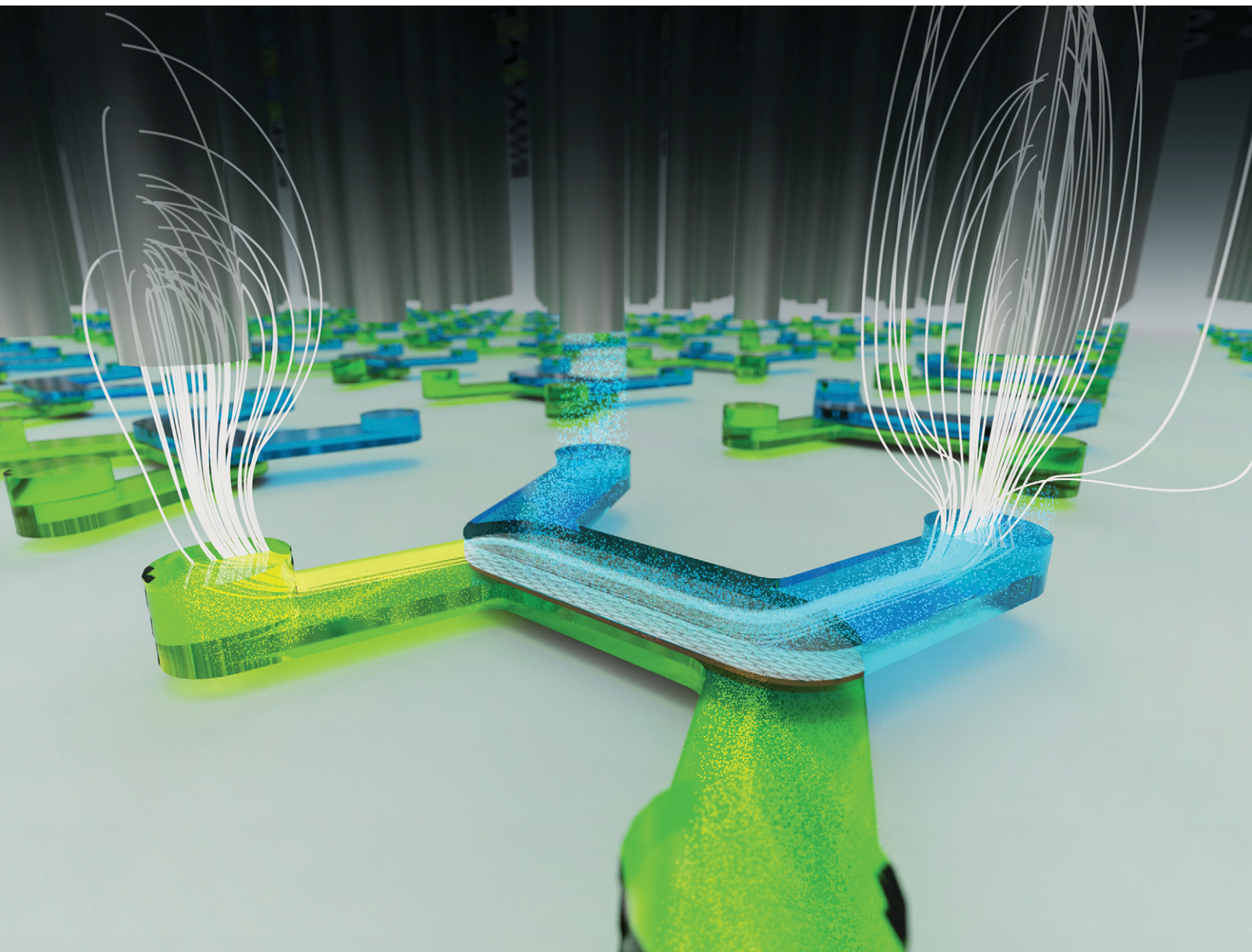


Lab on a Chip

Devices and applications at the micro- and nanoscale

rsc.li/loc



ISSN 1473-0197

PAPER

J. L. Charest *et al.*

High-throughput organ-on-chip platform with integrated programmable fluid flow and real-time sensing for complex tissue models in drug development workflows



Cite this: *Lab Chip*, 2021, **21**, 1454

High-throughput organ-on-chip platform with integrated programmable fluid flow and real-time sensing for complex tissue models in drug development workflows†

H. Azizgolshani,[‡]^a J. R. Coppeta,[‡]^a E. M. Vedula,[‡]^a E. E. Marr,^a B. P. Cain,^a R. J. Luu,^a M. P. Lech,^b S. H. Kann,^{ac} T. J. Mulhern,^a V. Tandon, K. Tan,^a N. J. Haroutunian,^a P. Keegan,^a M. Rogers,^a A. L. Gard,^a K. B. Baldwin,^a J. C. de Souza,^a B. C. Hoefer,^a S. S. Bale,^a L. B. Kratchman,^a A. Zorn,^a A. Patterson,^a E. S. Kim,^a T. A. Petrie,^a E. L. Wiellette,^a C. Williams,^a B. C. Isenberg and J. L. Charest ^{a*}

Drug development suffers from a lack of predictive and human-relevant *in vitro* models. Organ-on-chip (OOC) technology provides advanced culture capabilities to generate physiologically appropriate, human-based tissue *in vitro*, therefore providing a route to a predictive *in vitro* model. However, OOC technologies are often created at the expense of throughput, industry-standard form factors, and compatibility with state-of-the-art data collection tools. Here we present an OOC platform with advanced culture capabilities supporting a variety of human tissue models including liver, vascular, gastrointestinal, and kidney. The platform has 96 devices per industry standard plate and compatibility with contemporary high-throughput data collection tools. Specifically, we demonstrate programmable flow control over two physiologically relevant flow regimes: perfusion flow that enhances hepatic tissue function and high-shear stress flow that aligns endothelial monolayers. In addition, we integrate electrical sensors, demonstrating quantification of barrier function of primary gut colon tissue in real-time. We utilize optical access to the tissues to directly quantify renal active transport and oxygen consumption via integrated oxygen sensors. Finally, we leverage the compatibility and throughput of the platform to screen all 96 devices using high content screening (HCS) and evaluate gene expression using RNA sequencing (RNA-seq). By combining these capabilities in one platform, physiologically-relevant tissues can be generated and measured, accelerating optimization of an *in vitro* model, and ultimately increasing predictive accuracy of *in vitro* drug screening.

Received 27th January 2021,
Accepted 20th March 2021

DOI: 10.1039/d1lc00067e

rsc.li/loc



Introduction

Novel drug discovery efforts suffer from increasing costs and low probability of clinical trial success, largely due to a lack of predictive preclinical *in vitro* models^{1–4} and reliance on animal testing which often fails to accurately capture human response.^{5,6} To address this need, there has been an emergence of complex *in vitro* models that contain relevant aspects of human physiology.^{7–11} These models, which are collectively termed organ-on-chip (OOC) technology, have the

potential to greatly aid the development of new therapies.^{12–16} However, creating relevant components of human physiology is often achieved at the expense of throughput^{17,18} and the resulting technology is rarely directly compatible with industry standard workflow and infrastructure.¹⁹ A departure from this historical trade-off requires a new system architecture with advances in engineering and biology to create the next generation of organ-on-chip technology.

While current *in vitro* models do not fully recapitulate all aspects of the *in vivo* microenvironment, there is a strong body of literature indicating the physiologically relevant cues that guide tissue function; it is believed inclusion of such cues in an *in vitro* model will improve its ability to predict drug effects on humans. For instance, fluid flow *in vivo* influences tissue function by providing perfusion at lower flow rates^{20–23} and by additionally generating a flow-induced shear stress (FSS)^{24–27} at higher flow rates, highlighting the importance of including the capability to generate a range of

^aDraper, 555 Technology Square, Cambridge, MA 02139, USA.
E-mail: jcharest@draper.com

^bPfizer, Inc., 1 Portland Street, Cambridge, MA 02139, USA

^cDepartment of Mechanical Engineering, Boston University, 110 Cummington Mall, Boston, MA 02215, USA

† Electronic supplementary information (ESI) available. See DOI: 10.1039/d1lc00067e

‡ These authors contributed equally.

flow rates⁹ in OOC models. In addition, the spatial organization and chemical environment of cells influence tissue function; examples include heterotypic cell organization,²⁸ extra-cellular matrix (ECM) composition,²⁹ and spatial control of media composition and biochemical gradients to create distinct *in vivo* phenotypic zones.^{30,31} Additionally, maintaining near physiologic concentrations of autocrine and paracrine signals requires a low media-to-cell ratio within *in vitro* culture systems.³² OOCs that allow for integration of a diverse range of cell types, including those from various organs and with different qualification status, can increase the range of tissue model applications and cell sources. Incorporating these cues and features in an OOC enables selection of conditions to drive tissues toward physiologically accurate and, therefore, clinically predictive models.

The next generation of OOCs should improve upon standard *in vitro* models by integrating both new and established sensing modalities while maintaining compatibility with state-of-the-art data collection tools. Integrated sensors in OOCs can obtain real-time data over the course of an experiment^{17,18,33–35} without disturbing the microenvironment. While large data sets can be generated *in vitro* via high-throughput screening tools such as high-content screening (HCS) and RNA sequencing (RNA-seq), current OOC systems only interrogate one or a few tissue culture conditions³² in each experiment. We aimed to produce a next generation OOC system with on-line integrated sensing capabilities that maintains downstream compatibility with HCS and RNA-seq while enabling high-throughput interrogation of many tissue culture conditions simultaneously (or allows for a large number of replicates for a few culture conditions). Such a system will enable rapid parallel screening of many drug candidates and the generation of highly robust and complete data sets, including the ability to measure dynamic tissue behavior with previously inaccessible temporal resolution.

Here we present an advanced OOC platform technology that combines programmable flow control, integrated real-time sensors, and an ability to include heterotypic cell-type complexity within a high-throughput layout that readily interfaces with industry-standard infrastructure and state-of-the-art data collection tools. The platform comprises 96 individual OOC devices in one cell culture plate, up to 192 individual and actively-controlled micropumps contained within the plate lid, and 384 electrical contacts to make electrical measurements within each of the 96 devices.³⁶ Each OOC device contains two microchannels separated by a semi-permeable scaffold capable of supporting a range of cell types in mono- or co-culture to generate various tissue-relevant models. Fluid flow in each individual channel is controlled by a separate micropump with low fluid circuit dead volume to minimize dilution of cell-secreted factors. The platform employs optically clear thermoplastic materials chosen to minimize drug sorption and enable histological analysis using standard microscopy techniques. The format is compatible with existing life science

tools, including liquid and plate handling tools and assays, such as multiplex immunoassays, HCS and RNA-seq. In this manuscript, we demonstrate the versatility and broad capabilities of the platform by presenting a series of proof-of-concept experiments comprised of data from human kidney, vascular, liver, and intestine tissue models with relevant physiological readouts.

The models demonstrate distinct organ/tissue functionality, which is enabled by the novel features of the platform technology. Specifically, we demonstrate (a) two physiologically relevant flow regimes: perfusion flow that enhances hepatic tissue function and high-shear stress flow that aligns endothelial monolayers; (b) integrated electrical sensors that quantify barrier function of primary gut colon tissue in real-time; (c) optical access to the tissues that enables direct quantification of renal active transport and oxygen consumption; and (d) a format compatible with HCS and RNA-seq. These features, combined with the throughput capabilities, result in a platform that can both generate and interrogate microscale tissues and is expected to increase predictive accuracy of *in vitro* drug screening.

Results and discussion

Platform arrays microfluidics, active pumps, and sensors for simultaneous culture and analysis of 96 independent tissues

The organ-on-chip platform shown in Fig. 1 is comprised of three main components: (1) a thermoplastic microfluidic culture plate (MCP) in the standard well plate footprint with 96 individual devices, (2) a perfusion system incorporated into the lid of the MCP that contains up to 192 microfluidic pumps that individually address each device, and (3) a trans-epithelial electrical resistance (TEER) measurement system integrated with the perfusion system. The integrated perfusion and TEER systems are collectively termed as the micro-pump sensor array (MPSA). A rendered cutaway of the platform (Fig. 1a), shows the microfluidic channels of the MCP, and the microfluidic pumps and integrated TEER sensors of the MPSA. Pictures of the platform and its individual components is in ESI† Fig. S1, as well as a system block diagram that describes connection between the platform components.

(1) Device design and plate materials. Each of the 96 devices in the MCP consists of two overlapping microchannels, each with rectangular cross section (0.25 mm height, 1 mm width), and a track-etched microporous membrane that allows for physical and biological interactions between the microchannels (Fig. 1b and 2b). The inlets and outlets of each microchannel terminate at openings in the wells of a standard or custom 384-well plate, which serve as reservoirs for culture media. The custom version of the MCP (ESI† Fig. S3) enables a liquid-tight seal between standard pipette tips and the channel ports, which facilitates a filter-seeding method (ESI† Fig. S2), removal of potential bubbles trapped in the microchannels, and retrieval of media, cells, and genetic material from devices. The MCP



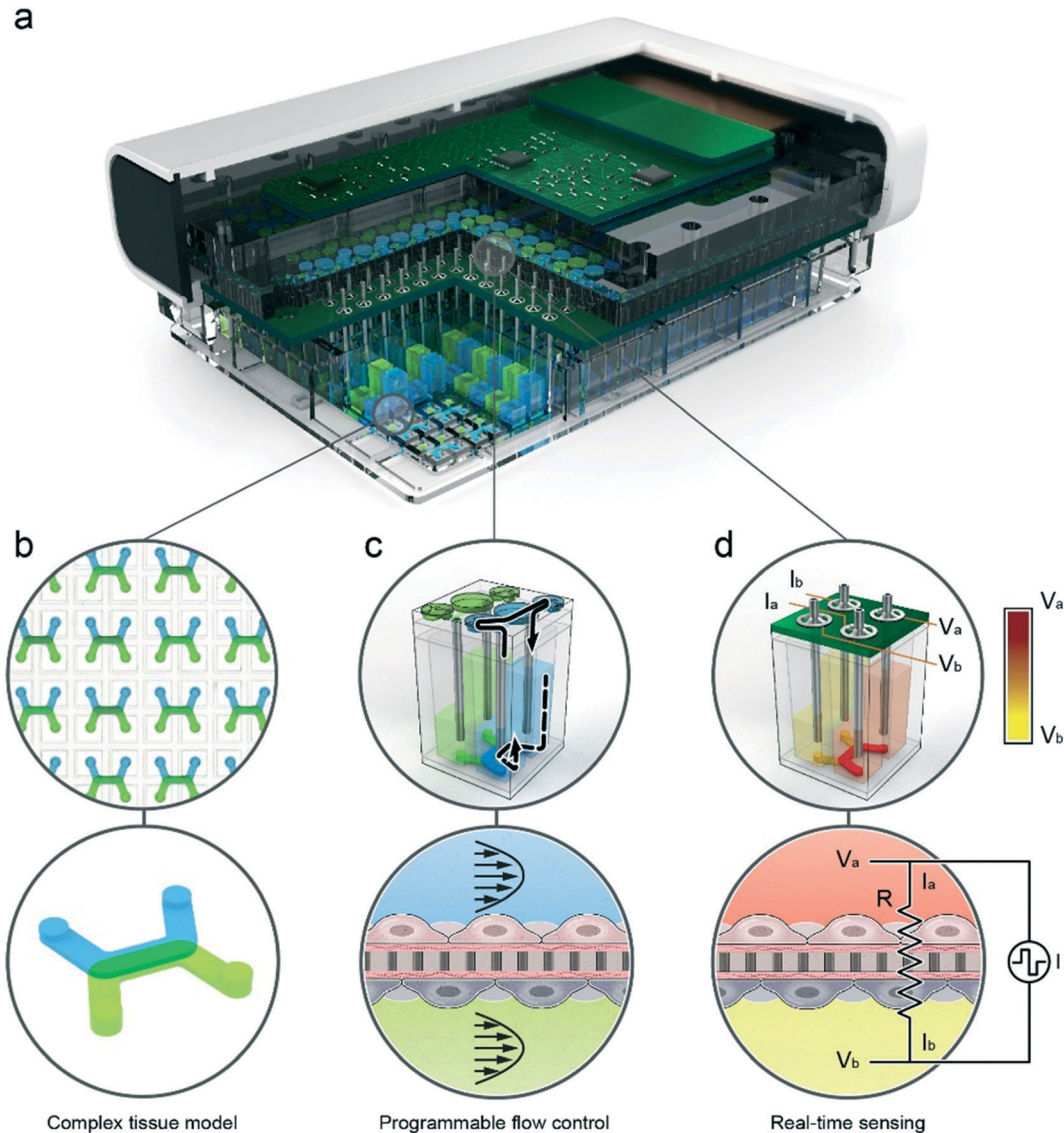


Fig. 1 High-throughput organ-on-chip platform with integrated pumping and sensing. **a**, A cutaway rendering of the platform shows the microfluidic channels of the MCP, and the micropumps integrated with the TEER electrodes and electronics of the MPSA. **b**, The MCP contains 96 independent microfluidic-based tissue models, each with two channels separated by a permeable membrane. The inlets and outlets of the top (blue) and bottom (green) channels are connected to 4 adjacent wells of a 384 well plate that serves as the media reservoir for each tissue model. The configuration of the channels allows for flexible co-culture of various cell types on either side of the membrane to develop complex tissue models. **c**, The micropumps are fluidically coupled to the wells of the MCP *via* vertical tubes that are submerged in the media reservoirs. Flow through each microchannel of the MCP is induced by an independent micropump. Micropumps transfer fluid between the interconnected wells, creating a pressure differential which in turn drives the fluid through the microchannel. **d**, For each device, the 4 associated micropump tubes serve as electrodes to enable a 4-point electrical measurement of the tissue resistance. One pair of submerged electrodes provides a biphasic current pulse across the tissue construct *via* a fluidic pathway, and a separate pair of electrodes sense electrical potential which can be used to calculate tissue resistance.

(ESI† Fig. S4) is constructed primarily from thin layers of cyclo-olefin polymers (COP), a thermoplastic material that offers a wide range of temperature grades, exhibits high transparency to light greater than 300 nm in wavelength, low autofluorescence, and low water absorption.^{37,38} For some experiments, a 125 μm layer of fluorinated ethylene propylene (FEP) was used at the bottommost layer of the MCP for its high oxygen permeability to allow for long-term static culture of the cells in the devices.^{36,39}

(2) Integrated pumping. In order to provide programmable fluid flow in the microchannels of the MCP, we designed an array of pneumatically-driven, self-priming micropumps positioned in the plate lid which are fluidically coupled to the MCP *via* a set of stainless steel vertical tubes that extend into the wells. The assembly of the micropump array is illustrated in ESI† Fig. S6. A single micropump, (Fig. 1c), recirculates media from the outlet well to the inlet well of a microchannel (solid arrow path) *via* the pneumatic actuation



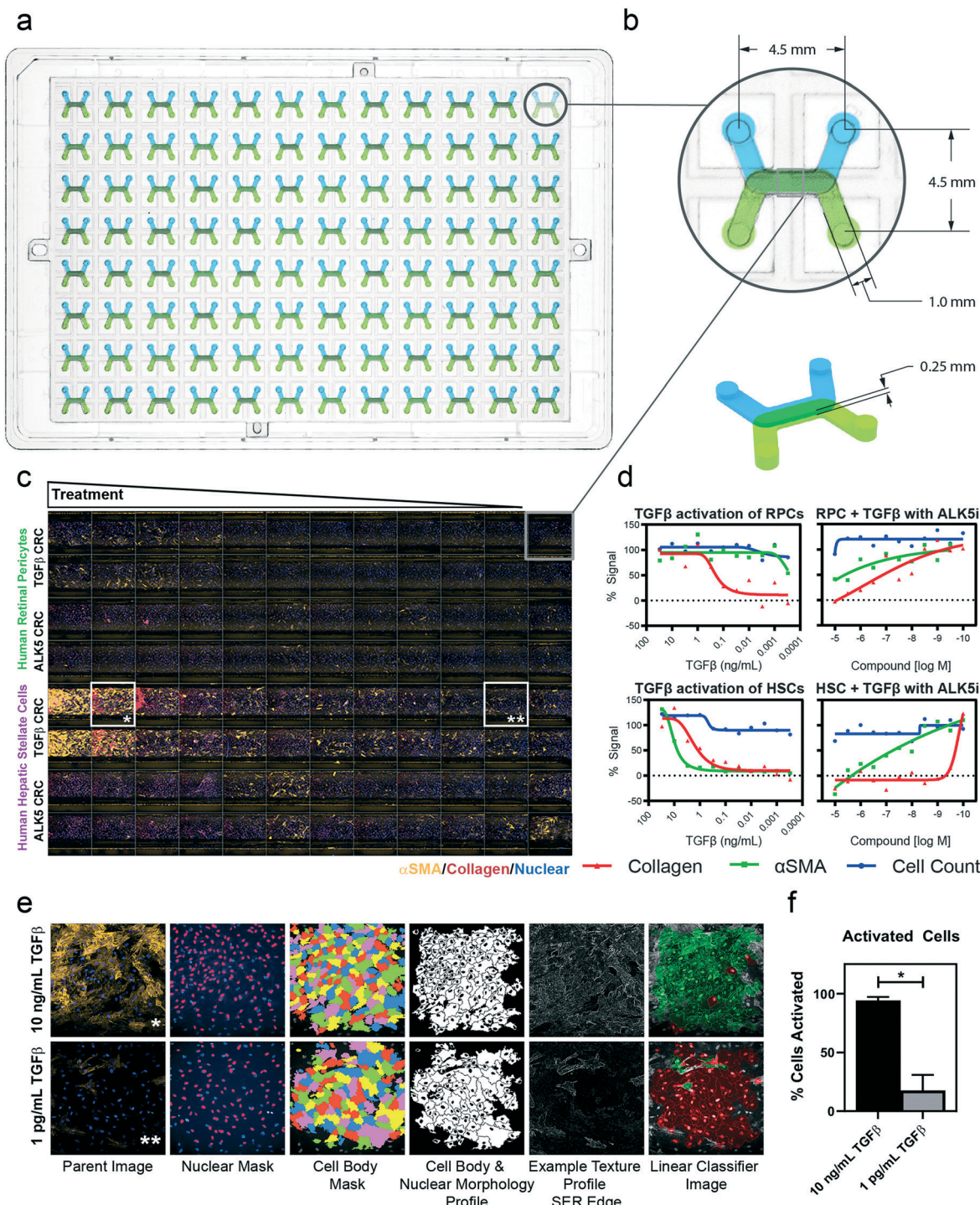


Fig. 2 The platform is compatible with high-content screening imaging systems and compound testing. **a**, The MCP has a standard well plate footprint, which enables compatibility with HCS systems **b**, each of the 96 devices is configured with a 4.5 mm inlet-outlet pitch and 0.25 mm channel height to enable compatibility with confocal imaging techniques. **c**, Representative panel from the Opera Phenix showing 3-color maximum intensity projection from Z-stack acquisition at 10 \times objective magnification, at the center of the channel overlap area for all 96 devices. Stains shown are α -smooth muscle actin (α SMA) (yellow), collagen 1 (red), and Hoechst 33342 (blue). Experiment depicts concentration response curves (CRC) of human retinal pericytes (RPCs, top half, $n = 48$) and human hepatic stellate cells (HSCs, bottom half, $n = 48$) to TGF β 1 with decreasing dose (rows A–B and E–F), 30 ng mL $^{-1}$ top, half-log dilutions. Rows C–D and G–H were treated with decreasing concentrations of an ALK5 inhibitor tool compound with a constant dose of 1 ng mL $^{-1}$ TGF β 1. **d**, Activation and inhibition curves of both conditions (TGF β activation, $n = 24$, and ALK5 inhibition, $n = 24$) for both cell types (RPCs and HSCs) with cell nuclear count, α SMA, and collagen readouts as percent signal of activated controls. **e**, 20 \times objective images of HSCs with 10 ng mL $^{-1}$ ($n = 1$, marked * in C) and 1 pg mL $^{-1}$ ($n = 1$, marked ** in C) treatments quantifying α SMA signal. Image processing sample images from left to right show the analysis sequence that was performed to generate high-content data using a linear classifying algorithm. **f**, High-content data for both devices imaged in **e**, showing the percentage of activated cells based on the linear classifier. Error bars represent standard deviations, * $p = 0.01$.

of a pair of valves and a pump chamber in a programmed sequence by the pump control unit (PCU) (ESI† Fig. S1b), as described in our previous works.^{11,40,41} The resulting change in the relative media volumes in each well establishes a hydrostatic pressure differential that induces flow of media through the microfluidic channels from the inlet well to the outlet well (dashed arrow path). Under steady-state conditions, the average flow rate generated in the MCP microchannels is equal to that of the micropumps. Pump flow rates are equal to the micropump stroke volume multiplied by the actuation frequency, which is set *via* a graphical user interface. In order to achieve a broad range of flow rates, two micropump chamber designs were implemented in the MPSA, the fluidic circuits of which can be seen in ESI† Fig. S5a and c, a 1.3 μL stroke volume micropump chamber used for models requiring only perfusion flow, and b and d, a 12 μL stroke volume micropump was used to achieve the high shear stresses needed to produce physiologically relevant vascular models (up to 7 dyn cm^{-2}). Implementation of the larger stroke volume (12 μL) design restricts the lid to 96 pumps while the perfusion flow (1.3 μL stroke volume) design allows for up to 192 micropumps in the lid.

To demonstrate ability of the MPSA system to provide uniform flow rates for each device, we have measured the pump stroke volumes within and between MPSAs over a period of one month under standard incubator conditions. The average stroke volumes of the 192 micropumps remained stable at $1.31 \pm 0.02 \mu\text{L}$ (ESI† Fig. S11). Details of the variation in stroke volume between individual micropumps in a single MPSA can be found in ESI† Fig. S9 and S10.

(3) Real-time sensing. To implement automated real-time and longitudinal TEER measurements in the MCPs, the stainless steel inlet and outlet micropump tubes of the lid were electrically connected to a multiplexing circuit, creating an array of 384 independent submerged electrodes, each addressing a single well of the plate (Fig. 1d). For each individual device, four of these electrodes were used to perform a 4-point impedance measurement with one pair of electrodes providing a biphasic current pulse across the tissue *via* a fluidic pathway and other pair of electrodes positioned in the remaining two wells to sense the electrical potential across the tissue (modeling and simulation results can be found in ESI† Fig. S14 and S15; electrode stability data can be found in ESI† Fig. S16). Each electrode is routed through a series of low-impedance multiplexer switches to an external analog measurement device. A graphical user interface enables the user to set experimental parameters as well as process and record live-acquired data. A TEER breakout board (TBB) provides necessary connections between components (ESI† Fig. S1b) by integrating the TEER measurement and micropumps into the MPSA system, measurements can in theory be made during an experiment in real-time in an incubator, maintaining the tissue environment and perfusion while minimizing factors that can destabilize TEER, such as temperature or pH fluctuations. For this manuscript, we made measurements outside the incubator so

we could better monitor operation of the system and ensure there were no bubbles, artifacts, or other sources of error in the system while measuring.

In the following sections we will demonstrate the integrated, broad capabilities of this OOC platform by presenting phenotypic data from our liver, vascular, gut/gastrointestinal, and kidney tissue models in a high-throughput format.

Optical access and microfluidic culture plate geometry enable high-content screening

Drug discovery and screening efforts frequently leverage imaging-based high-content screening (HCS) methods, rendering the adoption of OOC technology into the broader life science industry contingent upon compatibility with high-content imaging systems.^{42,43} Here, we demonstrate that the dual microchannel architecture and footprint of our platform is compatible with the standard software and hardware of an HCS system by analyzing our perivascular tissue model response to a pro-fibrotic trigger, transforming growth factor β (TGF β) (Fig. 2). The MCP was designed with a standard footprint and pitch of a traditional well plate (Fig. 2a). Each inlet and outlet of the 96 devices had a 4.5 mm spacing and were configured such that the cell-seeded membrane was parallel to the imaging slice of a confocal imaging system (Fig. 2b). The 0.25 mm channel height and bottom most material layer were chosen such that fluorescent imaging and laser reflectance Z-positioning could be used. Pericytes were imaged successfully, with good focus and fidelity of images achieved despite the optical path passing through the membrane. Each imaging run in the HCS system generated images from each of the 96 devices for a single field of view across 21 confocal microscopy z-planes using five laser wavelengths, yielding 10 080 total images in approximately 55 minutes. A 5 \times objective magnification covered greater than 90% of the channel overlap area, a 10 \times objective magnification covered ~33% of the channel overlap area, including the full width from channel wall to wall, and a 20 \times objective magnification covered ~10% of the device without capturing the walls in the image. Imaging time was scalable based on number of imaging locations for the 10 \times objective and 20 \times objectives and was not substantially different for the MCP compared to a standard 96 well plate.

Standard high-content workflows measure cell numbers based on nuclear count and fluorescence intensity to measure target-of-interest expression. Fluorescent labels were used to perform high-content analysis of the morphology and texture of the cells for use in linear classification. A representative panel (Fig. 2c) at 10 \times objective magnification and with a 3-color maximum intensity projection showed visible differences in protein expression across human retinal pericytes (RPCs, top half) and human hepatic stellate cells (HSCs, bottom half) to TGF β dose (decreasing dose rows A–B and E–F). Rows C–D and G–H were treated with decreasing concentrations of an ALK5 inhibitor tool compound with a constant dose of 1 ng mL^{-1} TGF β . EC₅₀ curves were generated to elicit the differential TGF β



activation of the two pericyte cell types and IC_{50} curves were generated to show compound inhibition of TGF β activation. The resulting curves showed no cytotoxicity in any condition, as indicated by negligible loss of cells in TGF β and ALK5i treatment conditions (Fig. 2d, blue curves). There was differential TGF β response between RPC and HSC populations as indicated by the α -smooth muscle actin (α SMA) and collagen EC 50 curves in Fig. 2d, first and third graphs. The IC 50 curves indicated that ALK5 inhibition of the HSCs and RPCs was different in terms of α SMA staining, but the compound dosing had similar effects on collagen inhibition (Fig. 2d, second and fourth graphs). A linear classifying algorithm was used with parameters from control populations of activated and non-activated cells to analyze the images obtained and processed *via* the standard Perkin-Elmer software (Fig. 2e). The high content readout performed as expected, quantifying α SMA positive cell populations with sufficient precision to clearly discern between activated and non-activated cells in the high (10 ng mL^{-1}) and low (1 pg mL^{-1}) TGF β doses, respectively (Fig. 2f).

Collectively, these data demonstrate that our platform is amenable to use on industry-accepted high-throughput, high-content screening/imaging systems, such as the PerkinElmer Opera Phenix, allowing for the adoption and use of the platform in both target-based and phenotypic screening regimes. High-throughput screening in some microfluidic culture platforms is possible,^{44,45} although only recently demonstrated with high-content screening analysis using a $10\times$ objective magnification objective.⁴⁶ While OOC can be used with customized or modified HCS strategies,⁴⁷ our platform leverages the power of existing HCS systems in their intended high-throughput format to analyze whole cells and sub-cellular structures by fitting existing HCS hardware, imaging mechanisms, analysis pipelines, and screening strategies. In addition, it will be ready to be used with new additions to HCS which can quantify genetic and proteomic changes.⁴⁸ The standard plate-based platform allows for the interaction of existing industry-based liquid handlers and robotics to fit all aspects of the analysis workflow, from seeding through imaging, streamlined and non-disruptive to currently established protocols.

Micro-pump sensor array (MPSA) system's user-controlled flow enhances tissue function

Fluid flow is known to drive tissue function through several mechanisms; examples include uni-directional flow for mechanobiological signalling in endothelial cells,^{49–51} and perfusion to maintain tissue homeostasis by controlling gradients of nutrients, oxygen, and waste.^{52,53} These mechanisms require an actively pumped system to control flow. Herein we demonstrate that the MPSA system is capable of providing uni-directional flow regimes ranging from low perfusion flow to high FSS flow and that these flow regimes directly affect tissue function.

Transporter qualified primary human hepatocytes display augmented metabolic enzyme activity under stable flow rate conditions. Perfusion is often critical to physiologic cell

function, for example physiologically-relevant media flow has resulted in elevated metabolic function and polarization of primary human hepatocytes (PHHs).^{54,55} In previous work, we demonstrated successful culture and robust cytochrome P450 3A4 (CYP3A4) activity of PHHs selected for ability to adhere.³⁶ To demonstrate response to flow of an additional hepatocyte type, we selected a transporter qualified hepatocyte which was not selected for ability to adhere. We used the custom MCP that integrates a tight fit between the inlet and outlet ports and the pipette tip thereby enabling the filter-seeding mechanism (ESI† Fig. S2 and S3, illustrated with colon cells), allowing robust control over seeding density. Transporter-qualified cells were seeded within the MCP and subjected to flow conditions from day 3 through 17 days of culture, and cytochrome activity was measured on days 3, 7, 13, and 17 using a luminogenic cytochrome P450 substrate detection kit for $N = 16$ at each day and condition. Cells seeded using the filter-assisted seeding mechanism attached to the scaffold, spread, and survived through 17 days of culture under both static and flow conditions in the MCP. The flow rate for these studies was selected to mimic physiologic mass transport of small proteins in the liver sinusoid by matching the Peclet number in our flow channel to the liver sinusoid Peclet number.⁵⁶ In addition, cells in flow conditions displayed stable cytochrome P450 activity (CYP1A2, CYP2B6, CYP3A4) through 17 days of culture, shown in Fig. 3b. Moreover, cells cultured under flow exhibited elevated activity of CYP3A4 and CYP2B6 on measurement days 7, 13, and 17 post-seeding, and CYP1A2 on days 7 and 17 at levels 50–200% higher than static conditions (Fig. 3b). Cells in static conditions received media changes every 48 hours.

By extending the timeline of tissue function *in vitro*, this platform affords a wider test window and enables chronic disease investigation. While we have previously demonstrated that flow in our platform augments hepatocyte health and CYP activity,³⁶ this study extends the effects of flow to hepatocytes qualified for transporter function but not qualified for ability to plate, which would render them difficult to use in OOC or other systems that require cell attachment. The filter-seeding technique enabled by the custom MCP allows the user to apply pressure across the membrane that resulted in adhesion of a PHH lot that was not selected for adhesion. This seeding method is in contrast to the standard MCP design, in which the user leverages hydrostatic pressure gradients to drive cells into the channel, resulting in cells settling onto the membrane by gravity. Given the significant number of human hepatocyte lots that are deemed difficult to use due to inability to plate, often the case for those sourced from diseased livers, this platform allows the potential use of a large contingent of previously untapped cell sources for drug discovery, toxicity and efficacy testing.

MPSA achieves physiologically-relevant FSS that induces endothelial cells alignment. Flow-induced shear stress is critical for vascular development and remodeling, and for maintenance of endothelial cell health and function, including modulation of cell responses to various stimuli.^{57,58} In this work, the MPSA with a larger stroke volume (12 μL) generated



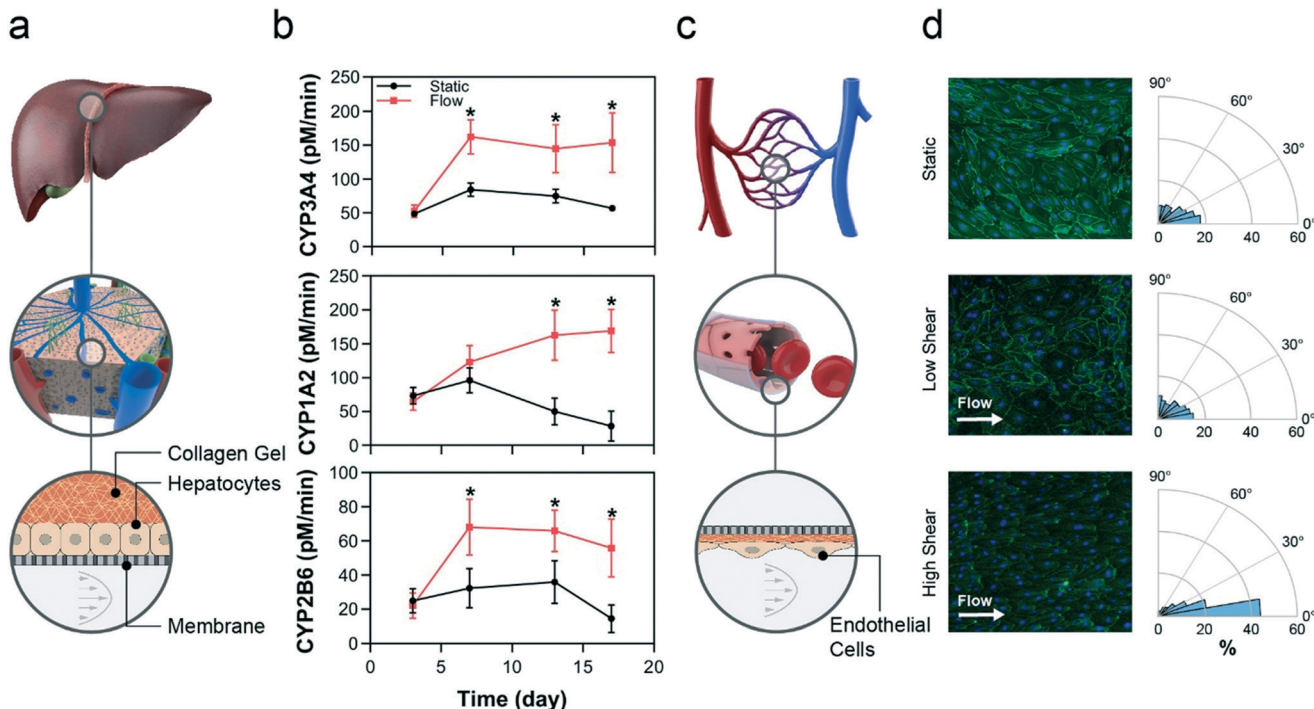


Fig. 3 Physiologically relevant fluid flow regimes alter tissue function and structure the platform. **a**, Primary human hepatocytes were configured in the MCP in a sandwich culture while the MPSA was able to supply perfusion flow to the bottom microchannel. **b**, Longitudinal activity of CYP3A4, CYP1A2, and CYP2B6 in hepatocyte cultures under either static or recirculating steady media flow ($50 \mu\text{L h}^{-1}$) conditions, administered beginning d3 in culture. * $p < 0.05$, flow vs. static, $N = 16$ replicates per data point. **c**, Primary human endothelial cells were cultured in the bottom microchannel of the MCP devices and exposed to FSS using the large stroke volume MPSA, with $N = 3$ for each condition. **d**, Representative images of endothelial monolayers stained for Hoechst (blue) and ZO-1 (green) for static (top), low (middle), and high fluid shear stress (bottom). Orientation of cell nuclei between $0\text{--}90^\circ$ was calculated relative to the direction of flow, with 0° indicating parallel alignment.

physiologically-relevant FSS, thereby providing the capability to simulate both pathological and healthy states. Here we leveraged the compatibility of the platform with common imaging modalities to quantify alignment and morphological changes of endothelial cells in response to FSS (Fig. 3c), providing a high-throughput means of establishing and assessing vascular health. Each condition has $N = 3$ replicates, allowing the remainder of the MCP to be used for control samples or other experiments. Immunofluorescence staining for the cell junction protein ZO-1 and Hoechst (Fig. 3d) showed robust monolayers of endothelial cells uniformly elongated in the direction of flow under high FSS. Analysis of nuclear alignment demonstrated an increase in the fraction of cells oriented parallel to the direction of flow under high FSS (7 dyn cm^{-2}) compared to static and low FSS (0.5 dyn cm^{-2}) as quantified in Fig. 3d. Overall, these data demonstrate that our platform can achieve a broad range of physiologically relevant fluid flow regimes to drive tissue-specific functions and responses.

Endothelial cells sense flow *via* mechano-sensing mechanisms, such as the PECAM-1/VEGFR2/VE-cadherin complex.^{59,60} Acknowledging that responses are EC subtype-specific, low FSS, defined here as less than 1.5 dyn cm^{-2} , typically induces inflammatory or other pathological responses in endothelial cells,⁶¹ whereas physiologic FSS, defined as $7\text{--}15 \text{ dyn cm}^{-2}$ in many *in vitro* systems, leads to cell-body and nuclear elongation, improved barrier function,

and reduced inflammatory marker expression.^{58,62,63} Higher-order cell functional changes can be inferred from endothelial cell elongation and orientation, which are standard metrics of EC function under FSS conditions.⁶⁴ These changes require a uni-directional flow of high enough sheer rate to be physiological, requiring an actively pumped system. Here, the changes in those standard metrics, which were appropriate for low and high FSS, show the ability of the pump system to generate flows and consequent tissue responses spanning diseased through healthy tissues for a range of endothelial subtypes.

Integrated sensing non-invasively monitors tissues in real-time

Real-time measurements allow investigators to optimize tissue performance, serve as a quality control metric, and examine mechanistic kinetics to gain a deeper understanding of tissue response to a number of factors. The integration of sensors enabled the non-destructive collection of data in a high-throughput format while minimizing disruption of environmental conditions and offering sampling rates sufficiently high to study dynamic behaviours.

Integrated electrical sensors quantify dose-dependent changes in intestinal barrier function. Barrier function, which is typically quantified using TEER measurements, is a key



metric that is widely used in assessing the health and performance of epithelial barriers, including intestinal tissue.^{65–67} Using arrayed TEER sensors, we tracked barrier function of our primary human intestinal epithelial model daily and in near real-time to demonstrate long-term and short-term barrier performance. The MPSA was capable of monitoring TEER in real-time, and when operating in a multiplexed data collection mode was able to measure each individual tissue model as frequently as once every 5 minutes to allow for sample stabilization and data processing. The MCP contained an experimental optimization matrix of 16 conditions (2 tissue types: left half, right half; 2 cell seeding techniques: top half, bottom half; and 4 media conditions: A/E, B/F, C/G, D/H) with 6 replicates per condition. During monolayer culture, cells were grown in proliferation medium (PM) for 4 days, and then transitioned into differentiation medium (DM). Specifically rows A, E transitioned from medium 4 to medium 2; rows B, F transitioned from medium 1 to medium 2; rows C, G transitioned from medium 1 to medium 3; and rows D, H transitioned from medium 1 to medium 1, with the various media defined in the materials and methods section. Tissue monolayers from intestinal tissue (Fig. 4a) were configured in the MCP to allow 4-point electrical resistance analysis (Fig. 4b). Outputs of the arrayed TEER system (Fig. 4c) consisted of 10 consecutive TEER measurements for each of the 96 devices at user-defined intervals for the entire duration of the experiment. From the individual TEER curves, the optimal conditions for proliferation and differentiation were selected and TEER curves reported for colon monolayers in those conditions (Fig. 4d, data from Fig. 4c B1–B6 and D1–D6). The transition into DM induced higher TEER readings (Fig. 4d), which typically reached a peak level and persisted through at least 11 days post-seeding. In both PM and DM, TEER begins to increase due to layers of cells becoming confluent. The higher TEER measured in DM correlated with cell-cell boundaries organizing into smoother and more continuous morphologies (Fig. 4e), reflecting a known association between TEER and tight junction formation.⁶⁸ While peak TEER values varied by experiment, in this instance colon monolayers gave a maximum TEER value of $234.5 \pm 33.7 \Omega \text{ cm}^2$ ($n = 5$, DM; $n = 6$, PM) on day 10 (Fig. 4d). Within a given set of conditions, the differentiated colon monolayers typically had higher TEER readings than undifferentiated colon monolayers. During TEER measurements the MCP was inspected and no sources of error, such as bubbles, leaks or lack of fluid connectivity, were found.

In addition to daily TEER measurements, we used the integrated TEER system to measure changes in barrier integrity over short time intervals in order to observe the kinetics of tissue response to an insult. We disrupted colon epithelial monolayers with doses of EGTA, a calcium chelator known to disorder intercellular junctions between epithelial cells.^{69,70} Quantification of TEER over time indicated a decrease in barrier function in response to EGTA exposure, as well as a dose-dependent recovery of barrier function upon reintroduction of calcium-containing medium (Fig. 4f). To correlate TEER with barrier function and the state of the

cells, we stained cultures with calcein AM to visualize monolayers after the treatment and recovery period. The monolayers treated with 30 mM EGTA contained rounded cells that were disconnected and non-confluent, while those treated with the 3.3 mM EGTA partially recovered their TEER values and had morphology similar to those in the untreated devices (Fig. 4g).

Although integration of TEER in culture systems has been demonstrated previously,^{17,71–73} few have integrated TEER for a high-throughput cell culture array, highlighting both the need and the apparent difficulty in developing such a system. Previously, TEER has been measured daily in a Caco-2 cell line in a 40-replicate OOC with rocker plate-induced flow.⁷⁴ Here, we have integrated the TEER system into a programmable, actively-pumped OOC, such that each of the 96 devices can be sampled in near real-time enabling *in situ* measurements that do not perturb the tissue. Colon tissue differentiated from primary human colon cells demonstrated the ability to characterize differentiation in a human-relevant model system using longitudinal TEER measurements. In addition, measuring TEER at a sampling rate on the order of minutes enabled evaluation of acute changes in barrier function and kinetics of the dosing and recovery responses. The integrated TEER sensors provided a non-destructive, near real-time measurement of barrier integrity that correlated to differentiation and barrier damage, while the overall platform enabled development of human-derived and donor-specific colon tissue models. Although used only for TEER here, the electrical probes of the TEER system could potentially be used to perform impedance spectroscopy quantifying electrical properties including capacitance and inductance, apply electrical stimulation, or integrate further biochemical detection by tethering functional chemistries to their surfaces.

Integrated oxygen sensors quantify kidney epithelial oxygen consumption and delivery of oxygen *via* flow. Dissolved oxygen concentration in culture influences many cellular functions and not only depends on cell-specific consumption rate, but the diffusive delivery of oxygen in the culture system. Quantification of oxygen consumption can provide insight into cellular metabolism while control over oxygen concentrations will support consistency throughout culture times and reproducibility across experiments. Here, we demonstrate the ability to measure dissolved oxygen in near real-time in devices cultured with kidney cells using an integrated oxygen sensor (Fig. 5a) under flow and static conditions. Primary human proximal tubule epithelial cells (hRPTEC) grew to confluence while under flow on the MCP membrane, as shown in Fig. 5b, in which the oxygen sensor appears as a dark circle. The oxygen sensor presence did not alter or restrict flow through the channel. Measurements across all 96 devices while the pump was operating at $10 \mu\text{L min}^{-1}$ demonstrated dissolved oxygen levels at or near saturation when oxygen was delivered *via* fluid flow. Upon stopping the pump in devices cultured with cells, oxygen levels dropped, as visualized in a single device (Fig. 5c), from 98% to 18% saturation over several hours (100% saturation is



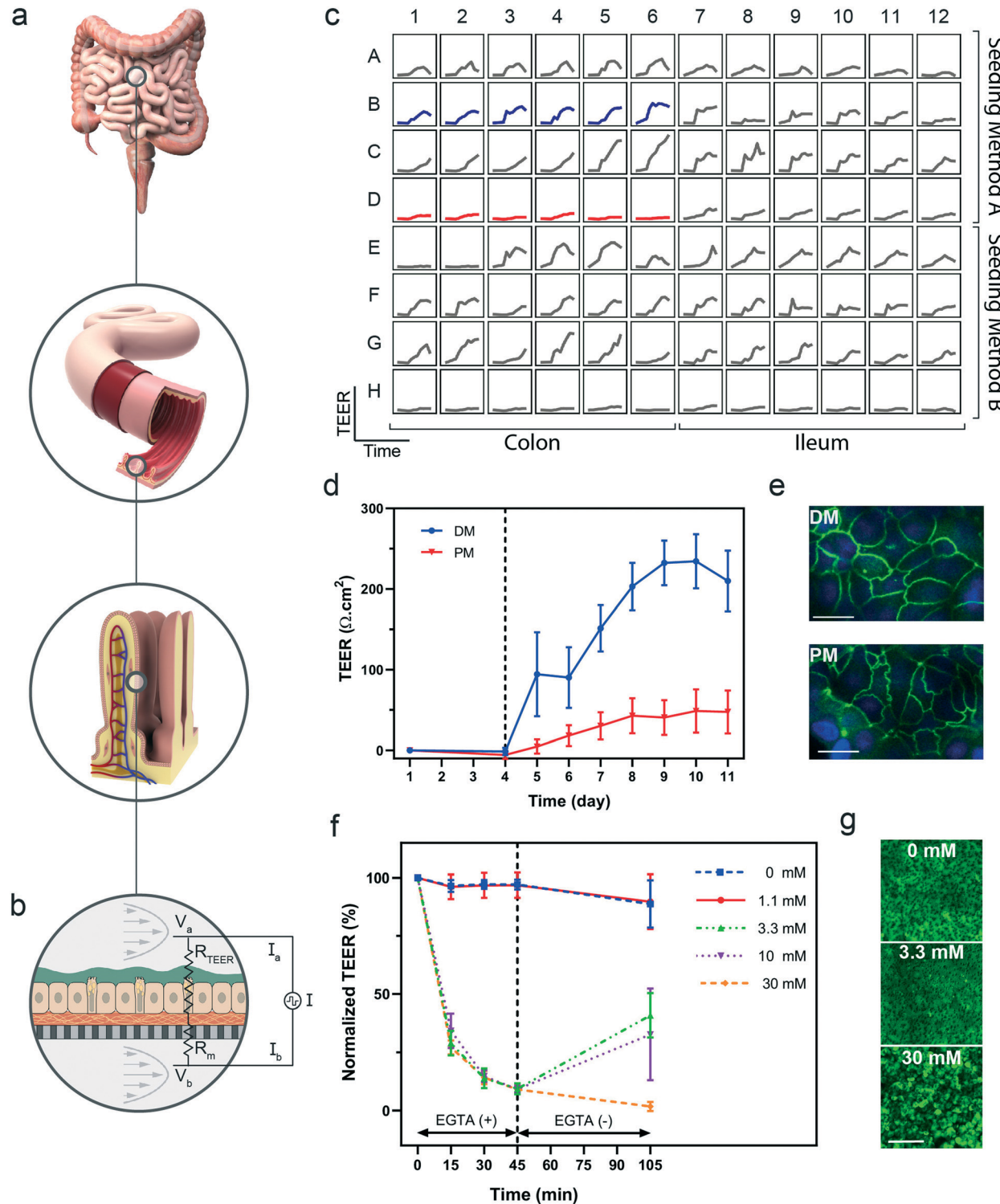


Fig. 4 Arrayed electrical sensing measures epithelial barrier function. **a**, *In vivo*, the intestinal epithelium provides a tight barrier that protects from luminal contents as well as controlling uptake of water and nutrients. **b**, Intestinal epithelial cell monolayers were grown in the MCP to quantify long-term and near real-time barrier function using four-point electrical resistance measurements. **c**, The MCP contained an experimental optimization matrix, which was designed to investigate TEER trends over time for 16 conditions, including two tissue types (left half, right half), two seeding methods (top half, bottom half) and four media types (A–D, E–H). **d**, Optimization led to selection of two conditions from those in **c**, TEER shown for the selected conditions in primary colon monolayers over 11 days post-seeding, where differentiation was induced on day 4 (dotted line), $n = 5$, DM; $n = 6$, PM. Error bars represent standard deviation from the mean. **e**, Cytoskeletal organization characterized by anti-zona occludens (ZO-1) immunofluorescence, comparing cells grown in DM (top) against those grown in PM (bottom). Scale bar represents 20 μm . **f**, Normalized TEER with respect to $t_0 = \text{EGTA} (+)$ and 60 minute recovery period. Error bars represent standard deviation from the mean, $n = 4$ per group. **g**, Calcein AM viability stain of cells in devices visualized 4 hours post treatment. Scale bar represents 200 μm .



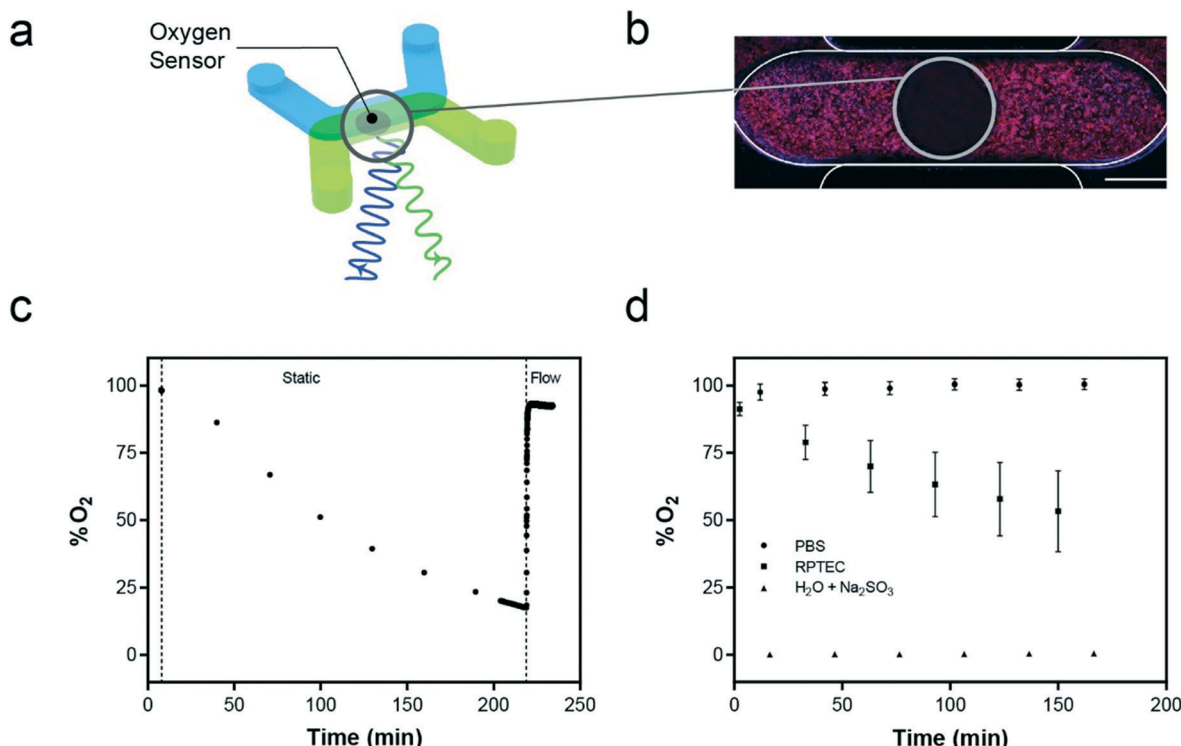


Fig. 5 Oxygen sensors integrated into the platform detect oxygen concentration in near real-time. **a**, The O₂ sensor spot, made from a photosensitive material, resides on the floor of the bottom microchannel of each of the devices in the MCP. The spot is interrogated with 620 nm wavelength and detected at 775 nm. **b**, hRPTEC stained with actin (red) and nuclei (blue) are visible on the membrane in the upper channel. The 0.75 mm diameter sensor spot obscures the signal from the cell staining and is seen as a dark circle. Scale bar = 0.5 mm. **c**, RPTECs cultured in a single device can consume over 75% of saturated oxygen levels over 220 minutes of static culture, which is triggered when the MSPA is shut off (first dotted line). Turning the MSPA back on (second dotted line) resulted in the relative O₂ concentration returning to 93% oxygen saturation. **d**, The average oxygen saturation level read by the integrated oxygen sensors were plotted for devices with PBS only (circle plot, $N = 60$), hRPTEC monolayers (square plot, $N = 27$), or water and sodium sulphite (triangle plot, $N = 4$) under static conditions. PBS alone retained 100% saturation O₂ concentration over 160 minutes. The presence of hRPTEC in the microchannel reduced relative O₂ concentration 46% over the same period. Sodium sulphite solution maintained a 0% O₂ concentration. Error bars represent standard deviations.

the oxygen concentration in cell culture medium when in equilibrium with atmospheric oxygen). When flow was reinitiated, the oxygen level increased rapidly to 93% saturation within 2 minutes and remained steady for the remaining duration of the test. Fig. 5d illustrates this same trend in devices cultured with hRPTEC ($N = 27$) compared to devices containing oxygenated PBS without any cells ($n = 60$), which remained at approximately 100% saturation and devices containing an oxygen quenching solution, sodium sulphite (Na₂SO₃) in water ($N = 4$), which served as a negative control and remained at approximately 0% oxygen saturation throughout the experiment. Average oxygen level across 27 devices containing hRPTEC declined from 91% to 53% saturation over 2.5 hours once pumps were stopped. 5 devices were removed from the total number of replicates due to bubbles in the channel, which would have otherwise biased oxygen measurements towards 100% saturation due to their inclusion of oxygen within the bubbles dissolving directly into the cell culture medium that was near the oxygen sensor.

While several groups have reported measuring oxygen in microfluidic tissue culture devices,^{21,75–79} such systems did

not integrate the sensors into a high-throughput format. The commercial Agilent Seahorse XFe96 Analyzer measures oxygen consumption rate for traditional 96 wellplates⁸⁰ but does not directly integrate with microfluidic OOC devices or allow for fluid flow. We have demonstrated we can measure the tissue oxygen environment in near real-time for each device in the MCP as well as maintain the oxygen saturation levels with fluid flow generated by the MFSP. While demonstrated here with hRPTECs, the ability to measure oxygen levels in the system and modulate delivery of oxygen *via* fluid flow enables environmental consistency despite cell-specific consumption rates. The integration of the oxygen sensing hardware with a standard microscope equipped with an incubation chamber enables control and maintenance of the culture environment during oxygen measurements, as well as the ability to conduct live cell imaging for multiplexed readouts from tissue samples. Our demonstration of optical access opens up opportunities to integrate additional optically-interrogable sensors to quantify other entities beyond oxygen. Optically-based sensors exist for pH, ions, glucose and other small entities whose transport to an optical sensing chemistry can be controlled *via* selectively permeable

polymer membranes.^{81–84} The platform could be expanded to these entities instead of or in addition to the oxygen sensors, yielding a multi-faceted label free readout of the culture conditions.

Device design enables quantification of drug-modulated active epithelial transport

Active transport of water and solutes, a main function of the kidney proximal tubule (Fig. 6a), influences drug toxicity and excretion. Here, we used the platform's optical access and low dilution volume to measure active transport across a kidney reabsorptive barrier. Primary human proximal tubule epithelial cells (hRPTEC) on the bottom of the membrane in the lumen microchannel and human microvascular endothelial (hMVEC) cells on top of the membrane in the vascular microchannel formed a co-culture (Fig. 6b) of proximal tubule-like barrier tissue, as demonstrated previously in a single unit OOC.⁸⁵ Under perfusion

conditions, the barrier function reached an average of $19 \Omega^* \text{cm}^2$ by day 3 and remained relatively constant until day 9. Monolayers of hRPTEC expressed significant organic anion transporter 1 (OAT1) (Fig. 6c) comparable to levels in the control hRPTEC TERT1 cell line, which constitutively expresses OAT1 (Fig. 6d). We introduced the fluorescent OAT1 substrate 6-carboxyfluorescein (6-CF) into the vascular microchannels, then quantified the amount of 6-CF transported into the lumen microchannels using real-time imaging. Fig. 6e–g depicts the intensity of 6-CF in the lumen channel for the three conditions tested, as seen through a $20\times$ microscope objective, with average intensity plotted in Fig. 6h. Devices with untreated cells on membranes had 30% lower intensity of 6-CF in the lumen microchannel when compared to devices with no cells on membranes, indicating the passive blocking of transport by the cells combined with some active transport. Probenecid treated cells on membranes had 6-CF levels 60% lower in the lumen microchannel than devices with no cells on membranes, in a

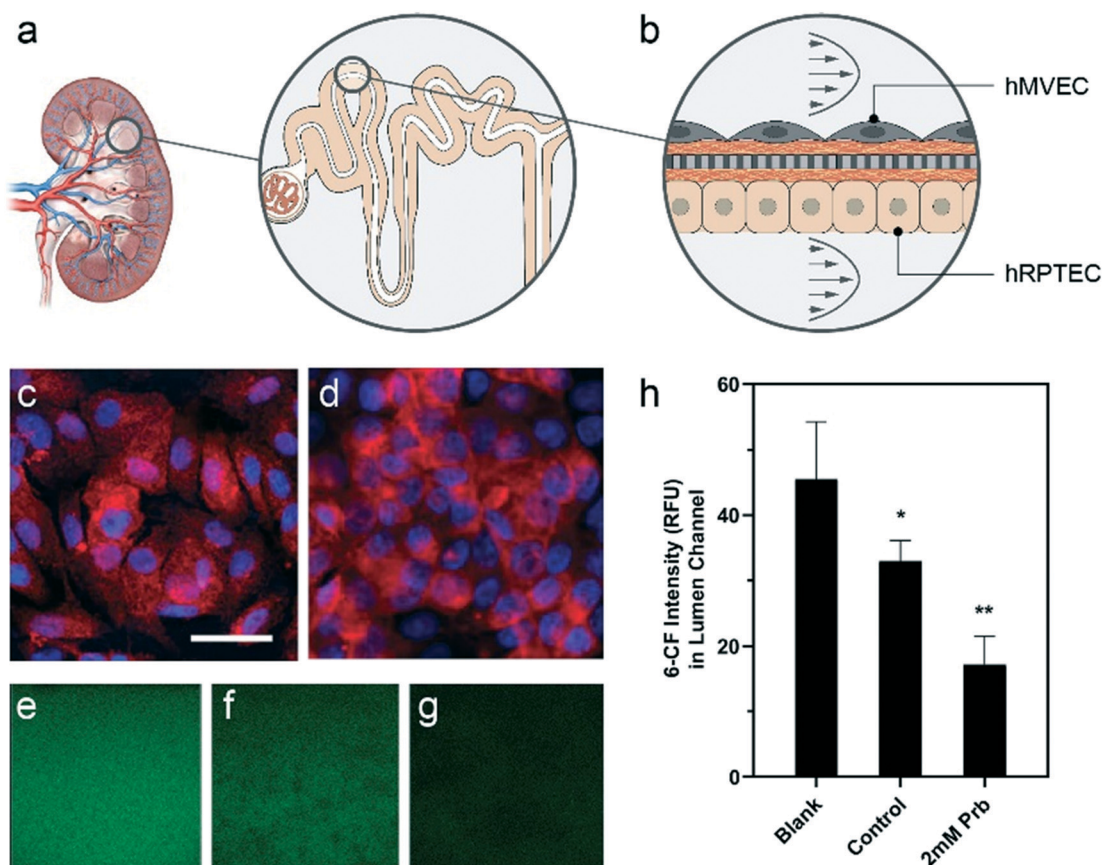


Fig. 6 Active transport can be directly quantified for a transport assay of the renal organic anion transporter 1 (OAT1). **a**, The renal proximal tubule is responsible for the majority of active transport in the kidney. **b**, hMVEC and hRPTEC were cultured on opposite sides of the membrane to form a complete reabsorptive barrier model. **c**, **d**, an hRPTEC/TERT1 cell line with stable expression of human OAT1 solute carrier (SLC) cultured in the platform stained for OAT1, red, and nuclei, blue, indicating presence of the OAT1 transporters. Scale bar represents $50 \mu\text{m}$. **e–g**, The intensity of fluorescent substrate, 6-CF, of OAT1 was quantified in lumen microchannels in blank (e, no cells), control (f, cells without probenecid) or 2 mM Prb (g, cells treated with probenecid) conditions using confocal z-stack and time-lapse microscopy. **h**, The bar graph shows the average fluorescent intensity of 6-CF in the lumen channel of devices and shows the significant reduction of active transport due to probenecid administration. Data are from 3 device replicates. Error bars represent standard deviation, $*p = 0.02$ with respect to blank, $**p < 0.009$ with respect to control.



manner consistent with active transport inhibition by probenecid,^{86,87} and reflecting both passive blocking of transport and a blockage of the active transport *via* OAT1.

Measuring active or passive transport across *in vitro* tissue cultures can be challenging as a result of the dilution effects from relatively high media volumes to cell numbers.^{88,89} The MCP microchannel design results in a 1 μ L microchannel volume which is small enough such that small changes in transport can be detected as measurable changes in concentration. The ratio of media volume to a cell is about 100 μ L per cell in the microchannel, which is within an order of magnitude of *in vivo* ratios (60 μ L per cell)⁹⁰ and significantly less dilute than a 96-well transwell, where 16 000 μ L per cell is expected from a typical seeding of 100 000 cells per cm^2 in an insert with 0.235 mL of cell culture media. Here, we take advantage of the low media volume to cell ratio to analyze transport *via* OAT1 in kidney proximal tubule cells. OAT1 is expressed in almost all epithelial barrier tissues in the body,⁹¹ but expression levels of OAT1 are the highest in the kidney, with localization in the basolateral membrane of proximal tubules.⁹² In the platform, the active transport of 6-CF, from the vascular channel to the luminal channel was optically tracked and analyzed in real-time, demonstrating the *in vitro* recapitulation of a physiologically relevant *in vivo* transport mechanism. The measurable yet incomplete reduction in 6-CF transport due to presence of cells on the membrane and further reduction due to the inhibitor indicated that 6-CF was impeded by a combination of passive paracellular and active transcellular/drug-modulated pathways. More dilute culture systems, like transwells, may necessitate use of cells with significantly reduced paracellular leak, which will limit cell selection^{93,94} and may not represent physiology of the tissue *in vivo*.⁹⁵ The format of our platform enabled the use of the desired cell type, flow-conditions to culture a multi-cell barrier over 7 days, and a quality check assessment of tissue barrier quality *via* integrated TEER to enable a quantitative measure of the active transport of substrates. The result is a demonstration of a functional response of tissue to a drug *in vitro* using primary cells.

Microchannels allow cell extraction for transcriptome analysis *via* RNA-seq

RNA-seq provides researchers with broad and unbiased profiles of the transcriptional states of cell populations, and is routinely used in multiple stages of drug discovery.⁹⁶ To demonstrate compatibility of our platform with RNA-seq, we seeded triplicates of retinal pericytes (RPCs) and retinal microvascular endothelial cells (RMVECs) into separate devices for six days of culture, removed them from the devices and sequenced total mRNA. Ability to distinguish between the two cell types based on mRNA expression of marker genes would indicate compatibility with the RNA-seq technique. At least 5 ng of RNA was collected from each device microchannel with at least RINe 7. The quantity and quality of the extracted RNA allowed each device to be

analyzed separately as opposed to pooling samples. Principal component analysis was able to clearly separate samples based on their cell types, as seen in Fig. 7a. Variance among replicates increased with the longer starvation condition, shown in the wider spread of the 24 h data with respect to PC2. A linear model was fit to transcript counts to measure differential expression between experimental conditions, and statistical significance was determined using a Wald test. Global differences between the RPC and RMVEC populations were visualized using an MA plot (Fig. 7b). Estimation of transcript counts correlated well between experimental replicates. Higher variance was observed at lower absolute counts, which is common for RNA-seq data, shown as a comparison between two experimental replicates (Fig. 7c). Each experimental replicate was a separate seeding of a unique MCP. Slight fabrication differences between devices within each MCP contribute to the technical variance observed in the experiment. To determine the effect of this added technical variance on the ability to measure differential expression, total variance was compared between cell types and culture conditions for the relatively lowly-expressed transcript NM_018057.6 of the amino acid transporter SLC6A15 (Fig. 7d). The transporter SLC6A15 was chosen since its low expression levels would be influenced more than more highly expressed transcripts by the added technical variance of the MCP variation, making this a relatively stringent test. Total variance between seeding replicates is shown along the x-axis. Quantification bootstraps were used to estimate the technical component of the variance and are plotted along the y-axis for each replicate. Despite the added technical variance from the MCPs, differential expression could clearly be observed between the RPC and RMVEC cell types for this lowly-expressed transcript. The top differentially-expressed transcripts between the cell types are easily visualized using a heat map (Fig. 7e).

RNA-seq analysis serves as a strict test of tissue model utility, since it can return data with potential to serve even clinical and regulatory roles if minimums for RNA quantity and quality⁹⁷ are achieved. Since OOC technologies often have total cell numbers less than traditional cell culture, they risk having insufficient RNA to perform a high quality analysis. The RNA-seq analysis here outputs data capturing a range of mRNAs. It demonstrates the ability to distinguish between known cell types with indications of sufficient quantity and quality of RNA output from the OOC platform. In addition, lowly-expressed transcripts with higher variance were still found to be differentially expressed between the two cell types. Based on this we expect any added variation from MPC devices would not limit use of RNA-seq in this platform. Finally, automated core sequencing facilities utilizing robotic liquid handlers to extract RNA, prepare libraries, and run sequencing pools in high throughput can interact with the OOC platform, ensuring the analytical pace matches that of other high-throughput analyses. The platform described here can integrate into such workflows,



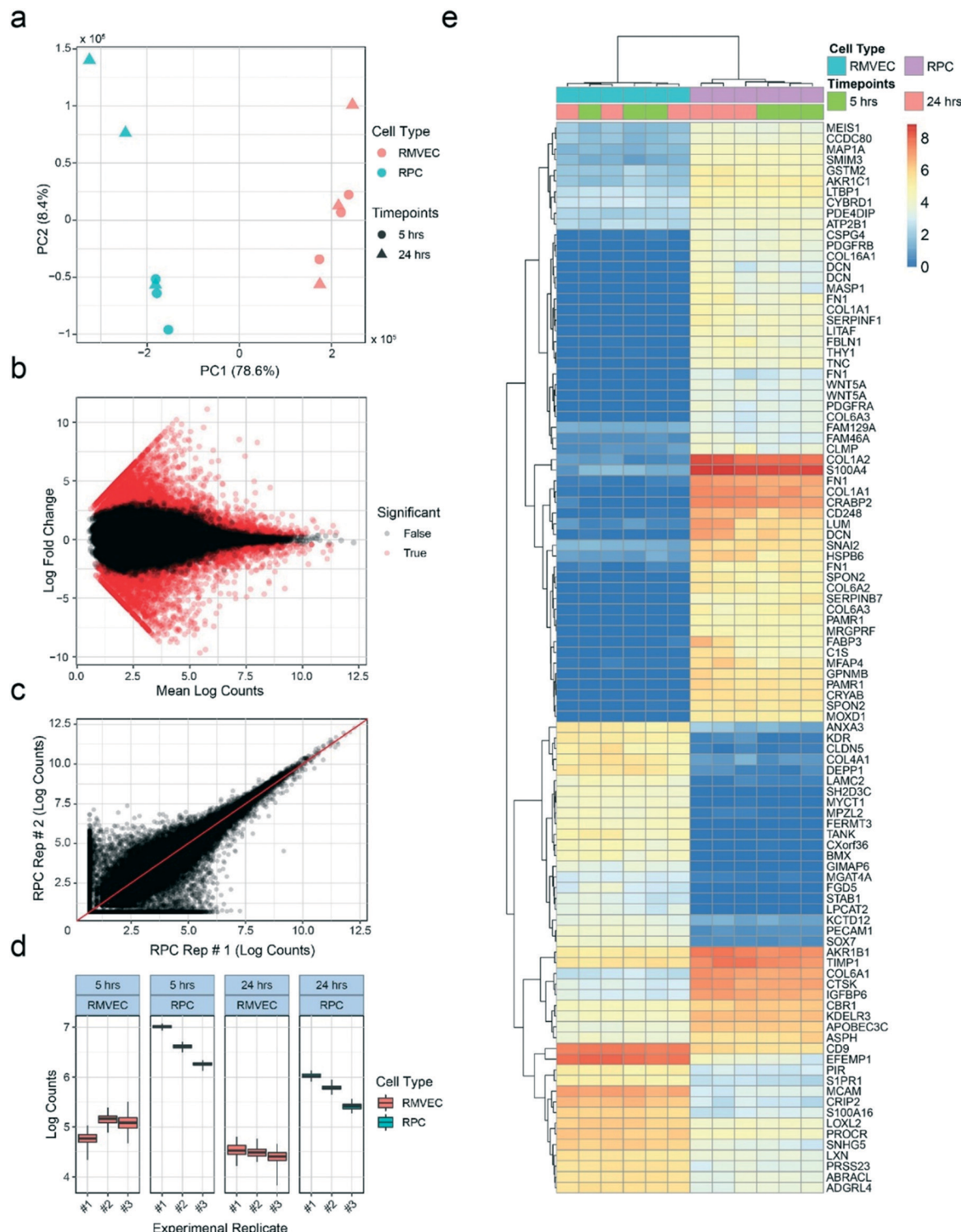


Fig. 7 RNA-seq analysis can quantify parameters of cells extracted from the OOC platform. **a**, Principal component analysis of normalized and filtered transcript counts for retinal pericytes (RPC) and retinal microvascular endothelial cells (RMVEC) from single channels of devices serum starved for 5 hours or 24 hours before analysis. The first two principal components are plotted. Clear separation of cell types is observed along the first principal component axis. **b**, MA plot of differential transcript abundances between RPCs and RMVECs. Log ratio is estimated from linear model coefficients. Log counts is normalized and filtered. Significance is based on an FDR threshold of 0.1. **c**, Normalized and filtered transcript counts for two RPC biological replicates (RPC Rep #1 and RPC Rep #2). Replicates correlate, with higher variance observed at lower mean expression, as is typical for RNA-seq experiments. **d**, Bootstrap analysis of technical variance for transcript NM_018057.6 of the amino acid transporter SLC6A15. The x-axis lists each biological replicate, which includes separate seedings of the 5 hour and 24 hour serum starve conditions. Three experimental replicates were used for differential expression analysis (3 seedings \times 2 starve conditions). **e**, Heat-map and hierarchical clustering between samples of normalized and filtered transcripts per million (TPM) shows a wide range of transcripts analyzed. Cell types are differentiated by known marker genes consistently for all biological replicates.



readily enabling studies that seek to test a large number of parameters, require a large number of replicates, or both.

Conclusions

We report a new OOC technology, the first to integrate low priming-volume pumps, user-programmable flow, sensing with real-time capability, and controlled heterotypic cell culture into a high-throughput format. This format is compatible with existing life science infrastructure for operation, such as automated liquid handling and plate shuttling, as well as for evaluation, such as high-content screening and RNA-seq. In addition, the design enables new seeding techniques that enhance the ability of cells to adhere and spread on the scaffold, allowing the use of cells that otherwise would not be possible to culture long term. Finally, the platform applies to a range of tissues, providing a means to influence as well as evaluate those tissues. Thus, the development of the innovative, integrated capabilities of the platform expands the potential uses of OOC and positions it to more broadly improve disease research and drug development.

Experimental

Microfluidic culture plate preparation

The microfluidic culture plates (MCP), fabricated as described in ESI† section “Fabrication of the microfluidic culture plate”, were prepared similarly for all experiments. First, the plates were treated with oxygen plasma for 1–5 minutes to render surfaces more hydrophilic. They were then sterilized by rinsing devices in ethanol and/or exposing the MCPs to UV light for 30 minutes. Individual devices were rinsed with water followed by PBS prior to coating channel surfaces with extracellular matrix proteins (hepatocytes: 20 $\mu\text{g mL}^{-1}$ human fibronectin and 20 $\mu\text{g mL}^{-1}$ rat tail collagen; endothelial cells: 5 $\mu\text{g mL}^{-1}$ human fibronectin; colon: 1:160 Matrigel; renal proximal tubule epithelial cells: 60 $\mu\text{g mL}^{-1}$ human collagen IV). In all microfluidic culture plates not coated with Matrigel, devices were rinsed with PBS following ECM deposition. Lastly, all MCPs were primed with model-specific cell culture media while cell suspensions were prepared for seeding.

Cell seeding

Cell seeding protocols varied slightly depending on cell type and application. Briefly, cells were either introduced into the device microchannels *via* a gravity seeding method using the standard MCP design (vascular ECs, kidney cells) or by a filter-seeding method in the custom MCP design (hepatocytes, colon cells). See ESI† Fig. S2–S4 for MCP design and corresponding seeding methods. For gravity methods (ESI† Fig. S2b), 35 μL and 15 μL of cell suspension (retinal pericytes and hepatic stellates at 250 000 cells per mL, vascular ECs at 500 000–1 000 000 cells per mL, proximal tubule cells at 1 500 000 cells per mL) were added to the inlet

and outlet wells of device microchannels, respectively. To culture cells below the scaffold, MCPs were flipped upside-down immediately after seeding for 1 hour. After cells adhered to the scaffold, additional media was added to the wells to bring the total volume to 75 μL . For filter-seeding methods (ESI† Fig. S2a), a tight-fit connection was made between the pipette tip and the custom MCP interface at both the inlet and outlet of the microchannel and 60 μL of cell suspension (hepatocytes at 500 000 cells per mL, colon at 400 000–1 000 000 cells per mL) was infused into the channel. The suspension media was convectively transported through the membrane into the adjacent channel while cells remained on the membrane. Cells were allowed to equilibrate briefly before the pipette tips were withdrawn from the ports. In all cases, MCPs were kept at 5% CO_2 and 37 °C and media was changed every 1 or 2 days. Specific methods on PHH suspension preparation and gut spheroid dissociation can be found in the ESI.†

High content screening assay

At 16 hours post-seeding, hepatic stellate cells (HSCs) were starved using stellate cell media containing a growth factor bullet for human stellate cells, 0.2% FBS and 1 \times penicillin-streptomycin (ScienCell, Cat. No. 5301) for 3–4 h prior to tool compound testing; retinal pericytes (RPCs) received fresh Quiescent Media. ALK5 inhibitor SB-431542, (ALK5i, Tocris) and human recombinant transforming growth factor β (TGF- β , R&D Systems) were solubilized according to vendor specifications at 30 mM and 20 $\mu\text{g mL}^{-1}$, respectively. Dose curves of each were prepared at 1000 \times final assay concentrations in 11 point half log dose curves with 30 μM for ALK5i and 30 ng mL^{-1} for TGF- β top final assay concentration. Dilutions were added to assay media for a 1 \times concentration and added to the respective inlet/outlet ports in a 75/15 μL addition scheme. After 72 hours, cells in the MCP were fixed and stained for high content screening of myofibroblast transition of both cell types across treatments. Plate definitions were established in Harmony (PerkinElmer) for high content imaging on an Opera Phenix High Content Screening System (PerkinElmer). All 96 devices on the MCP were imaged at 5 \times , 10 \times air, 20 \times air, and 20 \times water objectives to establish imaging processes for each hardware set up. Data presented in this paper are from 10 \times objective air (Fig. 2c) and 20 \times objective water (Fig. 2e) objectives. Briefly, imaging parameters were set for the center of each device with z-stacks to cover the full height on both sides of the membrane. Imaging for 5 channels (UV, Alexa 568, Alexa 647, Brightfield, Digital Phase Contrast) with individual exposure firing was completed. Image analysis was performed in Columbus (PerkinElmer) cloud-based high content imaging software. The analysis performed was standard intensity, morphology, and texture analysis. A custom linear classifier was also run within Columbus to utilize high content readouts of “activated” cells based on historic control populations. Intensity measurements were used to produce EC/IC₅₀ curves.



Morphology, texture, and the linear classifier were used to generate high content readouts of “% activated cells”.

Perfusion flow experiment in the liver model

Application of perfusion flow for the PHH model. Hepatocytes were cultured in a custom MCP with a FEP bottom and maintained under static conditions for 3 days prior to the initiation of perfusion flow. Media was changed every 24 hours. On the third day, a collagen I gel overlay was applied to the top channel, the MPSA system was primed with media, set to a flow rate of $50 \mu\text{L h}^{-1}$ in the bottom channel only, and connected to the custom MCP. Before being connected to the MCP, the MPSA underwent a priming step consisting of running the pump on a standard well plate full of cell culture medium. The priming step ensured consistency of circuit volume and eliminated the initial volume of air from being pumped into the device reservoir. Media was changed every 48 hours after day 3 for both static and flow conditions by replacing $100 \mu\text{L}$ of hepatic growth media in the bottom channel.

Cytochrome P450 (CYP) assays. All CYP assays were performed in static conditions during the assay. P450 activity was measured using the P450-Glo™ assay kits (Promega, CYP3A4: Cat. No. V9001; CYP1A2: Cat. No. V8421; CYP2B6: V8321), all modified for microfluidic culture plate use. For CYP1A2 and CYP2B6, 3 mM salicylamide was added to stock solutions to isolate phase I processes. For all assays, cultured PHHs were exposed to $60 \mu\text{L}$ of luciferin-CYP substrate in hepatocyte maintenance media by introducing it into the bottom channel and incubating at 37°C , 5% CO_2 for 90 minutes. Side-by-side comparisons of hepatocyte maintenance media and 0.1% dextrose-PBS in seeded devices yielded statistically minor differences in CYP levels, and so hepatocyte maintenance media was used for all subsequent studies to maintain robust cultures. At 30 min, 60 min, and 80 min, the substrate solution was mixed from inlet to outlet. At 90 minutes all media was collected and $25 \mu\text{L}$ added to $25 \mu\text{L}$ of detection reagent and luminescence measured after 10 minutes incubation at room temperature in the dark. CYP reaction rate was determined by comparing raw luminescence values to a standard curve generated using beetle luciferin (Promega, Cat. No. E1601). After the assay, the bottom channel was rinsed once with PBS, and $100 \mu\text{L}$ of new hepatocyte maintenance media was added to the bottom channel before restoration of perfusion flow and 37°C , 5% CO_2 incubation.

High shear flow experiment in the vascular model

Application of fluid shear stress. After cells attached and spread for 24 hours, the MPSA was placed on the MCP, after a priming step consisting of running the pump on a standard well plate full of cell culture medium. The priming step ensured consistency of circuit volume and eliminated the initial volume of air from being pumped into the device reservoir. Low flow was initiated at 0.5 dyn cm^{-2} ($48 \mu\text{L}$

min^{-1}). After 48 hour, high FSS of 7 dyn cm^{-2} ($600 \mu\text{L min}^{-1}$) was applied using the high shear MPSA while the low shear MPSA maintained low FSS conditions of 0.5 dyn cm^{-2} . FSS was applied to the bottom channel only, across MVEC monolayers. Devices under static (no flow) conditions received media changes every 2 days, as all devices under low and high FSS. Devices were fixed and stained 24 hours after the initiation of high shear.

Morphological analysis. Images of cells in device microchannels were processed using the Zen Black Tile Stitching tool. Briefly, images of the nucleus were run through a bandpass filter then thresholded. Nuclei were identified and labeled as connected components, then measured for orientation angle and eccentricity. Masks of the stitched tile images were generated using an adaptive histogram equalization algorithm combined with image intensity and size thresholding in MATLAB (MathWorks, R2018b). Cell orientation angle was calculated by taking the masks of the cell nuclei, fitting the image masks to an ellipse function, and determining the angle of the major axis of the ellipse relative to the flow direction which is parallel to the x -axis. An orientation of 0° indicates parallel alignment of nuclei relative to the direction of flow, whereas an orientation of 90° indicates nuclei alignment is perpendicular to the flow direction.

Barrier function experiments in the gut model

Long-term TEER assessment. Two seeding methods were investigated, called seeding method A and B. In method A, additional hydrostatic pressure was applied to the top channel immediately after seeding by adding $40 \mu\text{L}$ of media to the inlet. This is compared to the seeding method B, in which no additional media was added. Flow was initiated 1 day post-seeding at a flow rate of $60 \mu\text{L h}^{-1}$ utilizing the MPSA system. From day 1-3, monolayers were maintained in expansion medium. Differentiation was initiated on day 4 of culture by exchanging proliferation medium (PM) (composition as in ref. 93, with addition of 1 mM *N*-acetylcysteine, 10 mM Nicotinamide, 10 nM gastrin and 50 ng mL^{-1} human epithelial growth factor) with differentiation medium (DM) (composition as in ref. 93).^{98,99} Differentiation media was employed for the remainder of the experiment with media replenishment every other day. Specific formulations of PM and DM were used to select an optimal formulation. Specific media formulations are as follows: medium 1 consisted of 50% L-WRN conditioned medium, 10% fetal bovine serum, 40% Advanced DMEM/F12, 1× Pen/Strep, 1× GlutaMax, 10 μM Y27632, 10 μM SB431542, 10 mM HEPES, 1 mM *N*-acetylcysteine, 10 mM Nicotinamide, 10 nM Gastrin, 50 ng mL^{-1} EGF; medium 2 consisted of 75% Advanced DMEM/F12, 20% fetal bovine serum, 5% L-WRN conditioned medium, 10 mM HEPES, 1× Pen/Strep, 1× GlutaMax; medium 3 consisted of 5% L-WRN conditioned medium, 95% Advanced DMEM/F12, 1× Pen/Strep, 1× GlutaMax, 1 mM *N*-acetylcysteine, 10 mM HEPES, 10 nM



gastrin, 50 ng mL⁻¹ EGF, 10 μ M A83-01, 1× N-2 supplement, 1× B-27 supplement; medium 4 consisted of 50% L-WRN conditioned medium, 50% Advanced DMEM/F12, 1× Pen/Strep, 1× GlutaMax, 1 mM *N*-acetylcysteine, 10 mM HEPES, 10 nM Gastrin, 50 ng mL⁻¹ EGF, 10 μ M A83-01, 20 μ M Y27632, 1× N-2 supplement, 1× B-27 supplement. Longitudinal readings were taken every day up to and including 11 days on colon monolayers treated with DM ($n = 5$) and PM ($n = 6$) using the arrayed TEER sensors. The ROUT outlier test ($Q = 1\%$) was performed on data sets using GraphPad Prism 8.0 for each group of 6 replicate devices per time point of longitudinal TEER collected. The test defined one data point in the DM as an outlier on day 4 so it was removed from the presented data set in Fig. 4b and c for all time points. On days media was replenished, TEER measurements were taken outside the incubator and prior to media replenishment to minimize any artifacts of the media change and allow for inspection to rule out any artifacts that would affect TEER measurements such as presence of bubbles, leaks, or lack of fluid connection. The TEER measurements were used as a screening metric to identify optimal seeding methods for primary intestinal epithelial cells in the MCP.

Near real-time TEER assessment of barrier disruption. Prior to the cell seeding, blank TEER values were recorded in PBS for each device in the MCP. Primary colon monolayers were cultured in the MCP as previously described, and maintained without recirculating flow. At 6 days post seeding, the TEER of the monolayers was measured using the MPSA to establish a baseline reading prior to the introduction of ethylene glycol-bis(beta-aminoethyl ether)-*N,N,N',N'*-tetra acetic acid (EGTA). EGTA treatments were made up in Advanced DMEM/F12 media (stripped media) with HEPES buffer to yield concentrations of 30 mM, 10 mM, 3.3 mM, 1.1 mM, 0 mM EGTA. A control group was supplemented with DM in the event that stripped media caused a decrease in the barrier function of colon monolayers independent of calcium chelation. Experimental set-up yielded $n = 4$ for each EGTA concentration. After the introduction of EGTA, TEER was measured every 15 minutes. After the 45 minute time-point was recorded, the microchannels were aspirated and filled with DM to reintroduce calcium ions to the monolayers. Following 1 hour of the reintroduction of media, TEER was measured again to assess potential reestablishment of barrier function in colon monolayers after the reintroduction of calcium ions. All TEER measurements were taken outside the incubator in order to observe and rule out conditions that would alter TEER such as presence of bubbles, leaks, or lack of fluid connection after allowing the plate to equilibrate to room temperature over 15 minutes. Final TEER data was reported after subtracting blank values and normalizing to surface area. To assess viability, cells were stained with Calcein AM dye 4 hours after EGTA treatment. Calcein was diluted in cell culture media per supplier's recommendations, and cells were incubated with the dye solution for 30 minutes at 37 °C prior to *in situ* visualization using the microscope.

Oxygen sensor integration and analysis

An optical luminescence based oxygen sensing system was integrated with the platform for on-chip oxygen monitoring. Sensor spots (0.75 mm in diameter and 50 μ m thick) were cut with a biopsy punch from a sheet of photosensitive film (Pyroscience, Germany) and adhered to the center of each basal channel using silicone adhesive (Sylgard 184, Corning). A FireStingO2 optical oxygen meter (Pyroscience, Germany) with a fiber-optic cable was used to monitor oxygen in each device. During measurements, the platform was placed in an incubated confocal microscope and the fiber optic was secured parfocally onto the objective turret of the microscope using a custom fixture. The stage was programmed to align the fiber-optic with each sensor spot for O₂ monitoring in all 96 devices. A 2-point calibration of the FireStingO2 system was performed using devices filled with PBS equilibrated in air termed “100% saturation” and a “0% saturation” oxygen solution (30 g L⁻¹ sodium sulfite in water). Continuous oxygen measurements at a 1 Hz sampling rate were acquired in each device containing tissue under flow at 10 μ L min⁻¹. With flow stopped, single-point oxygen readings were acquired in each device every 30 minutes for 2.5 hours. During static to flow transition, oxygen was measured continuously at 1 Hz sampling rate in a single device as micropumps were turned on at 10 μ L min⁻¹.

Direct quantification of active transport in the kidney model

A co-culture of hRPTECs and hMVECs were cultured for 7 days under 10 μ L min⁻¹ of fluid flow. The transport of 6-carboxyfluorescein (6-CF), a fluorescent substrate of renal organic anion transporters, from the top/vascular channel to the bottom/lumen channel was characterized in 4 conditions: devices with no cells (no cell control), devices with cells (no drug control), devices with cells +1% DMSO (vehicle control), and devices with cells treated with 2 mM probenecid, a small molecule inhibitor of renal organic anion transport. Respective conditions were pretreated with media alone, vehicle or drug for 10 minutes prior to introducing 1 μ M 6-CF to the top channel. 6-CF was introduced in media, vehicle or drug solutions to maintain consistent conditions in each replicate. A Zeiss LSM 700 confocal microscope was programmed to couple z-stack and time-lapse imaging to acquire focal planes at 20 \times objective magnification in the bottom and top channel over 45 minutes at each device. Images taken in the bottom channel were analyzed for intensity of 6-CF substrate from all conditions.

RNA-seq analysis

RNA-seq analysis RPCs and RMVECs were cultured to confluence in static conditions (3–5 days), within the MCP, at which point they were starved by reduction of serum. Cells were detached from devices after 5 and 24 h post-starve using Accutase at 37 °C for 3–5 minutes. Devices were washed twice with 100 μ L media to collect detached cells. Cells were centrifuged and lysed with RLT buffer containing



2-mercaptoethanol. RNA was isolated following the Qiagen RNeasy Micro protocol with on-column DNaseI digestion and elution of RNA into a final volume of 14 μ L of water. RNA yield and integrity was evaluated using an Agilent Tapestation with high-sensitivity RNA ScreenTapes. Illumina libraries were prepared using the SMART-Seq v4 low-input protocol. Indexed libraries for each replicate were pooled and sequenced on a NextSeq 500 high-output flow cell with a single-ended 75 bp run configuration. Reads were processed by Kallisto¹⁰⁰ pseudoalignment against the NCBI GRCh38 human reference transcriptome. Pseudoalignments were further processed using Sleuth.¹⁰¹ Differential expression of transcripts between cell types was determined by a Wald test with an FDR threshold of 0.1.

Immunofluorescence staining and microscopy

Prior to immunofluorescence staining, devices were washed with PBS and cells were fixed using paraformaldehyde or methanol fixation for best results according to the target. For formaldehyde fixation, cells were fixed with 4% paraformaldehyde solution at room temperature for a period of 10–15 minutes. For methanol fixation, a solution of 95% methanol and 5% acetic acid at 4 °C was used. The devices were subsequently washed with PBS and formaldehyde fixed cells were permeabilized using 0.1% Triton-X solution at room temperature for 5–15 minutes. The cells were blocked with a suitable blocking buffer containing either 1% fetal bovine serum (FBS), 3% bovine serum albumin (BSA), or 3% normal goat serum (NGS) in PBS for a minimum of 1 hour at room temperature. Primary antibodies against targets of interest – α -smooth muscle actin (Millipore Sigma, clone 1A4, dilution 1:500), collagen I (Abcam, ab6308, 1:1000 dilution), ZO1 (BD Biosciences, 610967, dilution 1:250), OAT1 (ThermoFisher, PA5-26244, dilution 1:50) – were diluted in the blocking buffer and incubated overnight at 4 °C, and then washed using PBS or blocking buffer. Cells were then incubated with suitable fluorescently conjugated secondary antibodies at room temperature for 1–3 hours and washed with PBS. Cell nuclei were co-stained using Hoechst 33342 (ThermoFisher, 1:250 dilution from 1 mg mL⁻¹ solution). Further details for staining protocols for each specific model is provided in ESI.† Imaging was performed using a scanning confocal microscope (LSM700, Zeiss) equipped with 405 nm, 488 nm, 555 nm, and 637 nm lasers and 10 \times air, 20 \times air, and 40 \times water immersion objectives.

Competing interest

Work in this paper was partially supported by funding from Pfizer, Inc. who also participated in the research.

Author contributions

Hesham Azizgolshani: designed, conceived platform technology, performed simulations, led and executed engineering experiments, analyzed data, wrote manuscript. Jonathan R.

Coppeta: designed, conceived platform technology, performed simulations, led and executed engineering experiments, analyzed data, wrote manuscript. Else M. Vedula: designed, conceived platform technology, led and/or executed biological experiments, analyzed data, wrote manuscript. Elizabeth E. Marr: led and/or executed biological experiments, analyzed data, wrote manuscript. Brian P. Cain: designed platform technology, executed engineering experiments, analyzed data, wrote manuscript. Rebeccah J. Luu: led and/or executed biological experiments, analyzed data, wrote manuscript. Matthew Lech: led and/or executed biological experiments, analyzed data, wrote manuscript. Samuel H. Kann: led and/or executed biological experiments, analyzed data, wrote manuscript. Thomas J. Mulhern: led and/or executed biological experiments, analyzed data. Vishal Tandon: led and executed engineering experiments, analyzed data, wrote manuscript. Kelly Tan: led and/or executed biological experiments, analyzed data. Nerses J. Haroutunian: executed engineering experiments, analyzed data. Philip Keegan: supported platform development, executed biological experiments, analyzed data. Miles Rogers: led and/or executed biological experiments, analyzed data. Ashley L. Gard: led and/or executed biological experiments, analyzed data, wrote manuscript. Keith B. Baldwin: designed subset of platform technology. Jennifer de Souza: designed software/firmware for subset of platform technology. B. Christopher Hoefer: executed biological experiments, analyzed data, wrote manuscript. Shyam Bale: led and/or executed biological experiments. Louis Kratchman: designed, conceived platform technology. Alexander Zorn: designed subset of platform technology. Abigail Patterson: designed, conceived platform technology, led and executed engineering experiments. Ernest S. Kim: designed, conceived platform technology, wrote manuscript. Timothy A. Petrie: led and/or executed biological experiments, analyzed data. Elizabeth Wiellette: led and/or executed biological experiments, analyzed data, wrote manuscript. Corin Williams: led and/or executed biological experiments, analyzed data, wrote manuscript. Brett C. Isenberg: designed, conceived platform technology, performed simulations, led and executed engineering experiments, analyzed data, wrote manuscript. Joseph L. Charest: conceived platform technology, led engineering and biological experimental strategy, analyzed data, wrote manuscript.

Conflicts of interest

There are no conflicts to declare.

Acknowledgements

The authors would like to acknowledge significant contributors to the work. Anne M Ryan, Yvonne Will, Thomas A Wynn of Pfizer and Jeffrey T Borenstein of Draper for leadership and guidance. Lindsay Tomlinson, Michael Cain, Marion Kasaian, Celia Caballero-Franco, Eric Bauman, James R Gosset of Pfizer for technical input and participation in the research. Stephanie L Golmon and



Veronica C Newlin for design and fabrication development. Jason E Bahou and Yazmin N Obi for device fabrication. Alexander J Almeida and Ryan McGannon for electrical hardware and software assistance. Ryan S Maloney for assistance with biological experimentation. Jeffrey S Burrell and Robert J de St. Phalle for graphic design and artwork. The work was supported by Pfizer, Inc., The Charles Stark Draper Laboratory, and NSF Grant Award Number 1804845 (PI Charest).

References

- 1 J. W. Scannell, A. Blanckley, H. Boldon and B. Warrington, Diagnosing the decline in pharmaceutical R&D efficiency, *Nat. Rev. Drug Discovery*, 2012, **11**(3), 191–200.
- 2 D. Cook, D. Brown, R. Alexander, R. March, P. Morgan and G. Satterthwaite, *et al.*, Lessons learned from the fate of AstraZeneca's drug pipeline: a five-dimensional framework, *Nat. Rev. Drug Discovery*, 2014, **13**(6), 419–431.
- 3 J. A. DiMasi, L. Feldman, A. Seckler and A. Wilson, Trends in risks associated with new drug development: success rates for investigational drugs, *Clin. Pharmacol. Ther.*, 2010, **87**(3), 272–277.
- 4 C. H. Wong, K. W. Siah and A. W. Lo, Estimation of clinical trial success rates and related parameters, *Biostatistics*, 2019, **20**(2), 273–286.
- 5 H. Olson, G. Betton, D. Robinson, K. Thomas, A. Monroe and G. Kolaja, *et al.*, Concordance of the toxicity of pharmaceuticals in humans and in animals, *Regul. Toxicol. Pharmacol.*, 2000, **32**(1), 56–67.
- 6 M. Leist and T. Hartung, Inflammatory findings on species extrapolations: humans are definitely no 70-kg mice, *Arch. Toxicol.*, 2013, **87**(4), 563–567.
- 7 L. A. Low and D. A. Tagle, Tissue chips – innovative tools for drug development and disease modeling, *Lab Chip*, 2017, **17**(18), 3026–3036.
- 8 L. A. Low and D. A. Tagle, Tissue chips to aid drug development and modeling for rare diseases, *Expert Opin. Orphan Drugs*, 2016, **4**(11), 1113–1121.
- 9 K. Ronaldson-Bouchard and G. Vunjak-Novakovic, Organs-on-a-Chip: A Fast Track for Engineered Human Tissues in Drug Development, *Cell Stem Cell*, 2018, **22**(3), 310–324.
- 10 A. M. Holmes, S. Creton and K. Chapman, Working in partnership to advance the 3Rs in toxicity testing, *Toxicology*, 2010, **267**(1), 14–19.
- 11 S. Xiao, J. R. Coppeta, H. B. Rogers, B. C. Isenberg, J. Zhu and S. A. Olalekan, *et al.*, A microfluidic culture model of the human reproductive tract and 28-day menstrual cycle, *Nat. Commun.*, 2017, **8**, 14584.
- 12 P. Morgan, D. G. Brown, S. Lennard, M. J. Anderton, J. C. Barrett and U. Eriksson, *et al.*, Impact of a five-dimensional framework on R&D productivity at AstraZeneca, *Nat. Rev. Drug Discovery*, 2018, **17**(3), 167–181.
- 13 D. C. Swinney and J. Anthony, How were new medicines discovered?, *Nat. Rev. Drug Discovery*, 2011, **10**(7), 507–519.
- 14 M. Wagoner, J. Kelsal, M. Hattersley, K. Hickling, J. Pederson and J. Harris, *et al.*, Bromodomain and extraterminal (BET) domain inhibitors induce a loss of intestinal stem cells and villous atrophy, *Toxicol. Lett.*, 2014, **229**, S75–S76.
- 15 R. Barrile, A. D. van der Meer, H. Park, J. P. Fraser, D. Simic and F. Teng, *et al.*, Organ-on-Chip Recapitulates Thrombosis Induced by an anti-CD154 Monoclonal Antibody: Translational Potential of Advanced Microengineered Systems, *Clin. Pharmacol. Ther.*, 2018, **104**(6), 1240–1248.
- 16 D. Huh, B. D. Matthews, A. Mammoto, M. Montoya-Zavala, H. Y. Hsin and D. E. Ingber, Reconstituting Organ-Level Lung Functions on a Chip, *Science*, 2010, **328**(5986), 1662–1668.
- 17 S. Jeong, S. Kim, J. Buonocore, J. Park, C. J. Welsh and J. Li, *et al.*, A Three-Dimensional Arrayed Microfluidic Blood-Brain Barrier Model With Integrated Electrical Sensor Array, *IEEE Trans. Biomed. Eng.*, 2018, **65**(2), 431–439.
- 18 K. S. Bielawski, A. Leonard, S. Bhandari, C. E. Murry and N. J. Sniadecki, Real-Time Force and Frequency Analysis of Engineered Human Heart Tissue Derived from Induced Pluripotent Stem Cells Using Magnetic Sensing, *Tissue Eng., Part C*, 2016, **22**(10), 932–940.
- 19 S. J. Trietsch, G. D. Israëls, J. Joore, T. Hankemeier and P. Vullo, Microfluidic titer plate for stratified 3D cell culture, *Lab Chip*, 2013, **13**(18), 3548–3554.
- 20 Y.-C. Toh, T. C. Lim, D. Tai, G. Xiao, D. Noort and H. Yu, A microfluidic 3D hepatocyte chip for drug toxicity testing, *Lab Chip*, 2009, **9**(14), 2026–2035.
- 21 K. Rennert, S. Steinborn, M. Gröger, B. Ungerböck, A.-M. Jank and J. Ehgartner, *et al.*, A microfluidically perfused three dimensional human liver model, *Biomaterials*, 2015, **71**, 119–131.
- 22 B. Ataç, I. Wagner, R. Horland, R. Lauster, U. Marx and A. G. Tonevitsky, *et al.*, Skin and hair on-a-chip: in vitro skin models versus ex vivo tissue maintenance with dynamic perfusion, *Lab Chip*, 2013, **13**(18), 3555–3561.
- 23 M. Sato, N. Sasaki, M. Ato, S. Hirakawa, K. Sato and K. Sato, Microcirculation-on-a-Chip: A Microfluidic Platform for Assaying Blood- and Lymphatic-Vessel Permeability, *PLoS One*, 2015, **10**(9), e0137301.
- 24 A. Grassart, V. Malardé, S. Gobaa, A. Sartori-Rupp, J. Kerns and K. Karalis, *et al.*, Bioengineered Human Organ-on-Chip Reveals Intestinal Microenvironment and Mechanical Forces Impacting Shigella Infection, *Cell Host Microbe*, 2019, **26**(3), 435–444e4.
- 25 H. E. Abaci, Y.-I. Shen, S. Tan and S. Gerecht, Recapitulating physiological and pathological shear stress and oxygen to model vasculature in health and disease, *Sci. Rep.*, 2014, **4**(1), 1–9.
- 26 V. Raghavan, Y. Rbaibi, N. M. Pastor-Soler, M. D. Carattino and O. A. Weisz, Shear stress-dependent regulation of apical endocytosis in renal proximal tubule cells mediated by primary cilia, *Proc. Natl. Acad. Sci. U. S. A.*, 2014, **111**(23), 8506–8511.
- 27 Y. Duan, A. M. Weinstein, S. Weinbaum and T. Wang, Shear stress-induced changes of membrane transporter





localization and expression in mouse proximal tubule cells, *Proc. Natl. Acad. Sci. U. S. A.*, 2010, **107**(50), 21860–21865.

28 S. N. Bhatia, U. J. Balis, M. L. Yarmush and M. Toner, Effect of cell-cell interactions in preservation of cellular phenotype: cocultivation of hepatocytes and nonparenchymal cells, *FASEB J.*, 1999, **13**(14), 1883–1900.

29 P. D. Yurchenco, Basement membranes: cell scaffoldings and signaling platforms, *Cold Spring Harbor Perspect. Biol.*, 2011, **3**(2), 1–27.

30 H. Horsley, D. Dharmasena, J. Malone-Lee and J. L. Rohn, A urine-dependent human urothelial organoid offers a potential alternative to rodent models of infection, *Sci. Rep.*, 2018, **8**, 1238.

31 D. J. Felmlee, D. Grün and T. F. Baumert, Zooming in on liver zonation, *Hepatology*, 2018, **67**(2), 784–787.

32 J. P. Wikswo, F. E. Block, D. E. Cliffel, C. R. Goodwin, C. C. Marasco and D. A. Markov, *et al.*, Engineering challenges for instrumenting and controlling integrated organ-on-chip systems, *IEEE Trans. Biomed. Eng.*, 2013, **60**(3), 682–690.

33 B. Srinivasan, A. R. Kolli, M. B. Esch, H. E. Abaci and M. L. Shuler, Hickman JJ. TEER measurement techniques for in vitro barrier model systems, *J. Lab. Autom.*, 2015, **20**(2), 107–126.

34 B. M. Maoz, A. Herland, O. Y. F. Henry, W. D. Leineweber, M. Yadid and J. Doyle, *et al.*, Organs-on-Chips with combined multi-electrode array and transepithelial electrical resistance measurement capabilities, *Lab Chip*, 2017, **17**(13), 2294–2302.

35 Y. S. Zhang, J. Aleman, S. R. Shin, T. Kilic, D. Kim and S. A. M. Shaegh, *et al.*, Multisensor-integrated organs-on-chips platform for automated and continual in situ monitoring of organoid behaviors, *Proc. Natl. Acad. Sci. U. S. A.*, 2017, **114**(12), E2293–E2302.

36 K. Tan, P. Keegan, M. Rogers, M. Lu, J. R. Gosset and J. Charest, *et al.*, A high-throughput microfluidic microphysiological system (PREDICT-96) to recapitulate hepatocyte function in dynamic, re-circulating flow conditions, *Lab Chip*, 2019, **19**(9), 1556–1566.

37 A. Piruska, I. Nikcevic, S. H. Lee, C. Ahn, W. R. Heineman and P. A. Limbach, *et al.*, The autofluorescence of plastic materials and chips measured under laser irradiation, *Lab Chip*, 2005, **5**(12), 1348–1354.

38 R. K. Jena and C. Y. Yue, Cyclic olefin copolymer based microfluidic devices for biochip applications: Ultraviolet surface grafting using 2-methacryloyloxyethyl phosphorylcholine, *Biomicrofluidics*, 2012, **6**(1), 012822.

39 S. S. Bale, A. Manoppo, R. Thompson, A. Markoski, J. Coppeta and B. Cain, *et al.*, A thermoplastic microfluidic microphysiological system to recapitulate hepatic function and multicellular interactions, *Biotechnol. Bioeng.*, 2019, **116**(12), 3409–3420.

40 J. R. Coppeta, M. J. Mescher, B. C. Isenberg, A. J. Spencer, E. S. Kim and A. R. Lever, *et al.*, A portable and reconfigurable multi-organ platform for drug development with onboard microfluidic flow control, *Lab Chip*, 2016, **17**(1), 134–144.

41 V. Tandon, W. S. Kang, T. A. Robbins, A. J. Spencer, E. S. Kim and M. J. McKenna, *et al.*, Microfabricated reciprocating micropump for intracochlear drug delivery with integrated drug/fluid storage and electronically controlled dosing, *Lab Chip*, 2016, **16**(5), 829–846.

42 C.-W. Chi, A. R. Ahmed, Z. Dereli-Korkut and S. Wang, Microfluidic cell chips for high-throughput drug screening, *Bioanalysis*, 2016, **8**(9), 921–937.

43 Y. I. Wang, C. Carmona, J. J. Hickman and M. L. Shuler, Multi-Organ Microphysiological Systems for Drug Development: Strategies, Advances and Challenges, *Adv. Healthcare Mater.*, 2018, **7**(2), 1701000, available from: <https://www.ncbi.nlm.nih.gov/pmc/articles/PMC5805562/>.

44 L. Qiang, J. Guo, Y. Han, J. Jiang, X. Su and H. Liu, *et al.*, A novel anti *Candida albicans* drug screening system based on high-throughput microfluidic chips, *Sci. Rep.*, 2019, **9**(1), 8087.

45 G. Du, Q. Fang and J. M. J. den Toonder, Microfluidics for cell-based high throughput screening platforms—A review, *Anal. Chim. Acta*, 2016, **903**, 36–50.

46 V. van Duinen, D. Zhu, C. Ramakers, A. J. van Zonneveld, P. Vulto and T. Hankemeier, Perfused 3D angiogenic sprouting in a high-throughput in vitro platform, *Angiogenesis*, 2019, **22**(1), 157–165.

47 S. Peel, A. M. Corrigan, B. Ehrhardt, K.-J. Jang, P. Caetano-Pinto and M. Boeckeler, *et al.*, Introducing an automated high content confocal imaging approach for Organs-on-Chips, *Lab Chip*, 2019, 410–421.

48 M. Mattiazzi Usaj, E. B. Styles, A. J. Verster, H. Friesen, C. Boone and B. J. Andrews, High-Content Screening for Quantitative Cell Biology, *Trends Cell Biol.*, 2016, **26**(8), 598–611.

49 J. W. Song and L. L. Munn, Fluid forces control endothelial sprouting, *Proc. Natl. Acad. Sci. U. S. A.*, 2011, **108**(37), 15342–15347.

50 R. S. Reneman and A. P. G. Hoeks, Wall shear stress as measured in vivo: consequences for the design of the arterial system, *Med. Biol. Eng. Comput.*, 2008, **46**(5), 499–507.

51 R. S. Reneman, T. Arts and A. P. G. Hoeks, Wall shear stress – an important determinant of endothelial cell function and structure – in the arterial system in vivo, *J. Vasc. Res.*, 2006, **43**(3), 251–269.

52 M. D. Brennan, M. L. Rexius-Hall, L. J. Elgass and D. T. Eddington, Oxygen control with microfluidics, *Lab Chip*, 2014, **14**(22), 4305–4318.

53 P. E. Oomen, M. D. Skolimowski and E. Verpoorte, Implementing oxygen control in chip-based cell and tissue culture systems, *Lab Chip*, 2016, **16**(18), 3394–3414.

54 L. Prodanov, R. Jindal, S. S. Bale, M. Hegde, W. J. McCarty and I. Golberg, *et al.*, Long Term Maintenance of a Microfluidic 3-D Human Liver Sinusoid, *Biotechnol. Bioeng.*, 2016, **113**(1), 241–246.

55 M. Hegde, R. Jindal, A. Bhushan, S. S. Bale, W. J. McCarty and I. Golberg, *et al.*, Dynamic interplay of flow and collagen stabilizes primary hepatocytes culture in a microfluidic platform, *Lab Chip*, 2014, **14**(12), 2033–2039.

56 K. Tan, J. Coppeta, H. Azizgolshani, B. C. Isenberg, P. M. Keegan and B. P. Cain, *et al.*, Correction: A high-throughput microfluidic microphysiological system (PREDICT-96) to recapitulate hepatocyte function in dynamic, re-circulating flow conditions, *Lab Chip*, 2020, 1556–1566.

57 N. Baeyens, S. Nicoli, B. G. Coon, T. D. Ross, K. Van den Dries and J. Han, *et al.*, Vascular remodeling is governed by a VEGFR3-dependent fluid shear stress set point, *eLife*, 2020, 4, e04645, available from: <https://www.ncbi.nlm.nih.gov/pmc/articles/PMC4337723/>.

58 L. Cucullo, M. Hossain, V. Puvenna, N. Marchi and D. Janigro, The role of shear stress in Blood-Brain Barrier endothelial physiology, *BMC Neurosci.*, 2011, 12, 40.

59 D. Conway and M. A. Schwartz, Lessons from the endothelial junctional mechanosensory complex, *F1000 Biol. Rep.*, 2012, 4, 1, available from: <https://www.ncbi.nlm.nih.gov/pmc/articles/PMC3251317/>.

60 B. G. Coon, N. Baeyens, J. Han, M. Budatha, T. D. Ross and J. S. Fang, *et al.*, Intramembrane binding of VE-cadherin to VEGFR2 and VEGFR3 assembles the endothelial mechanosensory complex, *J. Cell Biol.*, 2015, 208(7), 975–986.

61 A. Ishibazawa, T. Nagaoka, H. Yokota, S. Ono and A. Yoshida, Low shear stress up-regulation of proinflammatory gene expression in human retinal microvascular endothelial cells, *Exp. Eye Res.*, 2013, 116, 308–311.

62 A. Ishibazawa, T. Nagaoka, T. Takahashi, K. Yamamoto, A. Kamiya and J. Ando, *et al.*, Effects of shear stress on the gene expressions of endothelial nitric oxide synthase, endothelin-1, and thrombomodulin in human retinal microvascular endothelial cells, *Invest. Ophthalmol. Visual Sci.*, 2011, 52(11), 8496–8504.

63 M. B. Simmers, A. W. Pryor and B. R. Blackman, Arterial shear stress regulates endothelial cell-directed migration, polarity, and morphology in confluent monolayers, *Am. J. Physiol.*, 2007, 293(3), H1937–H1946.

64 J. Shao, L. Wu, J. Wu, Y. Zheng, H. Zhao and Q. Jin, *et al.*, Integrated microfluidic chip for endothelial cells culture and analysis exposed to a pulsatile and oscillatory shear stress, *Lab Chip*, 2009, 9(21), 3118–3125.

65 O. Y. F. Henry, R. Villenave, M. Cronce, W. Leineweber, M. Benz and D. E. Ingber, Organs-on-Chips with integrated electrodes for Trans-Epithelial Electrical Resistance (TEER) measurements of human epithelial barrier function, *Lab Chip*, 2017, 17(13), 2264–2271.

66 C. M. Costello, M. B. Phillipsen, L. M. Hartmanis, M. A. Kwasnica, V. Chen and D. Hackam, *et al.*, Microscale Bioreactors for in situ characterization of GI epithelial cell physiology, *Sci. Rep.*, 2017, 7(1), 12515.

67 J. Costa and A. Ahluwalia, Advances and Current Challenges in Intestinal in vitro Model Engineering: A Digest, *Front. Bioeng. Biotechnol.*, 2019, 7, 1–14, available from: <https://www.frontiersin.org/articles/10.3389/fbioe.2019.00144/full#B30>.

68 S. Varadarajan, R. E. Stephenson and A. L. Miller, Multiscale dynamics of tight junction remodeling, *J. Cell Sci.*, 2019, 132(22), jcs229286, available from: <https://jcs.biologists.org/content/132/22/jcs229286>.

69 G. Samak, D. Narayanan, J. H. Jaggar and R. Rao, CaV1.3 Channels and Intracellular Calcium Mediate Osmotic Stress-induced N-terminal c-Jun Kinase Activation and Disruption of Tight Junctions in Caco-2 Cell Monolayers, *J. Biol. Chem.*, 2011, 286(34), 30232–30243.

70 G. Samak, T. Suzuki, A. Bhargava and R. K. Rao, c-Jun NH2-terminal kinase-2 mediates osmotic stress-induced tight junction disruption in the intestinal epithelium, *Am. J. Physiol.*, 2010, 299(3), G572–G584.

71 J. Yeste, M. Garcia-Ramirez, X. Illa, A. Guimera, C. Hernandez and R. Simo, *et al.*, A compartmentalized microfluidic chip with crisscross microgrooves and electrophysiological electrodes for modeling the blood-retinal barrier, *Lab Chip*, 2017, 18(1), 95–105.

72 H. Xu, Z. Li, Y. Yu, S. Sizdahkhani, W. S. Ho and F. Yin, *et al.*, A dynamic in vivo-like organotypic blood-brain barrier model to probe metastatic brain tumors, *Sci. Rep.*, 2016, 6(1), 36670, available from: <http://www.nature.com/articles/srep36670>.

73 K. Hiramoto, K. Ino, Y. Nashimoto, K. Ito and H. Shiku, Electric and Electrochemical Microfluidic Devices for Cell Analysis, *Front. Chem.*, 2019, 7, available from: <https://www.frontiersin.org/article/10.3389/fchem.2019.00396/full>.

74 C. Beaurivage, E. Naumovska, Y. Chang, E. Elstak, A. Nicolas and H. Wouters, *et al.*, Development of a Gut-on-a-Chip Model for High Throughput Disease Modeling and Drug Discovery, *Int. J. Mol. Sci.*, 2019, 20(22), 5661.

75 S. Jalili-Firoozinezhad, F. S. Gazzaniga, E. L. Calamari, D. M. Camacho, C. W. Fadel and A. Bein, *et al.*, A complex human gut microbiome cultured in an anaerobic intestine-on-a-chip, *Nat. Biomed. Eng.*, 2019, 3(7), 520–531.

76 H. Zirath, M. Rothbauer, S. Spitz, B. Bachmann, C. Jordan and B. Müller, *et al.*, Every Breath You Take: Non-invasive Real-Time Oxygen Biosensing in Two- and Three-Dimensional Microfluidic Cell Models, *Front. Physiol.*, 2018, 9, available from: <https://www.frontiersin.org/article/10.3389/fphys.2018.00815/full>.

77 A. Moya, M. Ortega-Ribera, X. Guimerà, E. Sowade, M. Zea and X. Illa, *et al.*, Online oxygen monitoring using integrated inkjet-printed sensors in a liver-on-a-chip system, *Lab Chip*, 2018, 18(14), 2023–2035.

78 D. Bavli, S. Prill, E. Ezra, G. Levy, M. Cohen and M. Vinken, *et al.*, Real-time monitoring of metabolic function in liver-on-chip microdevices tracks the dynamics of mitochondrial dysfunction, *Proc. Natl. Acad. Sci. U. S. A.*, 2016, 113(16), E2231–E2240.

79 S. A. Mousavi Shaegh, F. De Ferrari, Y. S. Zhang, M. M. Nabavinia, N. Binth Mohammad and J. Ryan, *et al.*, A microfluidic optical platform for real-time monitoring of pH and oxygen in microfluidic bioreactors and organ-on-chip devices, *Biomicrofluidics*, 2016, 10(4), 044111.

80 M. Koopman, H. Michels, B. M. Dancy, R. Kamble, L. Mouchiroud and J. Auwerx, *et al.*, A screening-based platform for the assessment of cellular respiration in *Caenorhabditis elegans*, *Nat. Protoc.*, 2016, 11(10), 1798–1816.



81 K. J. Cash and H. A. Clark, Nanosensors and nanomaterials for monitoring glucose in diabetes, *Trends Mol. Med.*, 2010, **16**(12), 584–593.

82 W. Di and H. A. Clark, Optical nanosensors for in vivo physiological chloride detection for monitoring cystic fibrosis treatment, *Anal. Methods*, 2020, **12**(11), 1441–1448.

83 G. Rong, E. E. Tuttle, A. Neal Reilly and H. A. Clark, Recent Developments in Nanosensors for Imaging Applications in Biological Systems, *Annu. Rev. Anal. Chem.*, 2019, **12**(1), 109–128.

84 G. Rong, E. H. Kim, Y. Qiang, W. Di, Y. Zhong and X. Zhao, *et al.*, Imaging Sodium Flux during Action Potentials in Neurons with Fluorescent Nanosensors and Transparent Microelectrodes, *ACS Sens.*, 2018, **3**(12), 2499–2505.

85 E. M. Vedula, J. L. Alonso, M. A. Arnaout and J. L. Charest, A microfluidic renal proximal tubule with active reabsorptive function, *PLoS One*, 2017, **12**(10), e0184330, available from: <https://www.ncbi.nlm.nih.gov/pmc/articles/PMC5636065/>.

86 M. A. Nagle, D. M. Truong, A. V. Dnyanmote, S.-Y. Ahn, S. A. Eraly and W. Wu, *et al.*, Analysis of Three-dimensional Systems for Developing and Mature Kidneys Clarifies the Role of OAT1 and OAT3 in Antiviral Handling, *J. Biol. Chem.*, 2011, **286**(1), 243–251.

87 C. Zou, (*RPTEC/TERT1*) Modified to Express Drug Transporter – ATCC, 2017.

88 J. P. Wikswo, E. L. Curtis, Z. E. Eagleton, B. C. Evans, A. Kole and L. H. Hofmeister, *et al.*, Scaling and systems biology for integrating multiple organs-on-a-chip, *Lab Chip*, 2013, **13**(18), 3496–3511.

89 H. E. Abaci and M. L. Shuler, Human-on-a-chip design strategies and principles for physiologically based pharmacokinetics/pharmacodynamics modeling, *Integr. Biol.*, 2015, **7**(4), 383–391.

90 J. Graf, A. Gautam and J. L. Boyer, Isolated rat hepatocyte couplets: a primary secretory unit for electrophysiologic studies of bile secretory function, *Proc. Natl. Acad. Sci. U. S. A.*, 1984, **81**(20), 6516–6520.

91 S. K. Nigam, K. T. Bush, G. Martovetsky, S. Y. Ahn, H. C. Liu and E. Richard, *et al.*, The organic anion transporter (OAT) family: a systems biology perspective, *Physiol. Rev.*, 2015, **95**(1), 83–123.

92 M. Roth, A. Obaidat and B. Hagenbuch, OATPs, OATs and OCTs: the organic anion and cation transporters of the SLCO and SLC22A gene superfamilies: OATPs, OATs and OCTs, *Br. J. Pharmacol.*, 2012, **165**(5), 1260–1287.

93 A. H. Heussner and D. R. Dietrich, Primary porcine proximal tubular cells as an alternative to human primary renal cells in vitro: an initial characterization, *BMC Cell Biol.*, 2013, **14**(1), 55.

94 K.-W. Zhao, E. J. B. Murray and S. S. Murray, HK2 Proximal Tubule Epithelial Cells Synthesize and Secrete Plasma Proteins Predominantly Through the Apical Surface, *J. Cell Biochem.*, 2017, **118**(4), 924–933.

95 P. Claude and D. A. Goodenough, Fracture faces of zonulae occludentes from “tight” and “leaky” epithelia, *J. Cell Biol.*, 1973, **58**(2), 390–400.

96 A. Doostparast Torshizi and K. Wang, Next-generation sequencing in drug development: target identification and genetically stratified clinical trials, *Drug Discovery Today*, 2018, **23**(10), 1776–1783.

97 Illumina. TruSeq® RNA Sample Preparation v2 Guide [Internet]. Illumina, 2014, Available from: https://support.illumina.com/content/dam/illumina-support/documents/documentation/chemistry_documentation/samplepreps_truseq/truseqrna/truseq-rna-sample-prep-v2-guide-15026495-f.pdf.

98 T. Sato, D. E. Stange, M. Ferrante, R. G. J. Vries, J. H. van Es and S. van den Brink, *et al.*, Long-term Expansion of Epithelial Organoids From Human Colon, Adenoma, Adenocarcinoma, and Barrett's Epithelium, *Gastroenterology*, 2011, **141**(5), 1762–1772.

99 H. Miyoshi and T. S. Stappenbeck, In vitro expansion and genetic modification of gastrointestinal stem cells in spheroid culture, *Nat. Protoc.*, 2013, **8**(12), 2471–2482.

100 N. L. Bray, H. Pimentel, P. Melsted and L. Pachter, Near-optimal probabilistic RNA-seq quantification, *Nat. Biotechnol.*, 2016, **34**(5), 525–527.

101 H. Pimentel, N. L. Bray, S. Puente, P. Melsted and L. Pachter, Differential analysis of RNA-seq incorporating quantification uncertainty, *Nat. Methods*, 2017, **14**(7), 687–690.

